Chiral Symmetry Breaking in Four-fermion Interaction Model with Thermal and Finite-size Effects

Theoretical Particle and Hadron Physics Group,
Graduate School of Science, Hiroshima University

Hiromu Shimoji

2022

Abstract

Symmetry is a basic concept in physics. It is expected that a higher symmetric phase is realized in the early universe and the symmetry spontaneously breaks down to the one of the standard model in particle physics through the spacetime evolution. Chiral symmetry plays an important role in the mechanism of dynamical mass generation for matter. It is significant to reveal the phase structure in terms of the chiral symmetry. The phase structure is ordinarily illustrated on a chemical potential-temperature (μ-T) plane in high-energy physics and it is well known that the structure varies with the physical conditions of the surrounding environment. The study of the effects of various environments can lead to a better understanding of phase structures. Here, we focus on finite-size effects on chiral symmetry breaking in strongly coupled systems of fermions.

Four-fermion interaction models are often used to describe spontaneous breaking of the chiral symmetry. At first, we briefly review the four-fermion interaction models at zero temperature and a finite temperature. In this thesis, the Gross–Neveu model is basically employed as the simplest of these models of the chiral symmetry breaking. Evaluating the effective potential in the leading order of the $1/N$ expansion, we investigate the phase structure with the finite-size effect.

We discuss the phase structure with the finite-size effect at zero temperature. In the previous works, the divergent part of the effective potential are simply removed along with a finite part that depends on parameters of the system. We improve the procedure and evaluate the effective potential, the dynamically generated fermion mass and the string tension. In addition to the phase transition, we discuss a stable size of the system. The phase structure are independent of the improvement, but the string tension is modified. The search for the stable size of the system under the string tension revealed that the stable size is not realized.

Next, we consider the thermal effect in addition to the finite size effect. Caused by the finite-size effect, more complex phase structures are realized at a finite temperature and a finite chemical potential. In order to investigate the precise phase structure, we evaluate not only the minimum but also for the other extrema of the effective potential. Through the analysis, we show the phase diagrams on parameter planes. Complex structures of boundaries is found at a certain size of the system for a low temperature and a high chemical potential. We also evaluate the behavior of the thermodynamic quantities and find the stable size of the system.

Contents

Chapter 1

Introduction

It is well-known that the following four interactions are fundamental in physics: strong, electromagnetic and weak interactions and gravity. The standard model in particle physics describing the three interactions except for the gravity has great successes, for example, the prediction of the Higgs boson and its discovery. These interactions in the standard model are described quantum field theories based on a gauge symmetry, $\mathrm{SU}(3)_c \times \mathrm{SU}(2)_L \times \mathrm{U}(1)_Y$. Quarks and leptons that construct matters are obtained as fundamental representations of the group. Although the standard model has brilliantly succeeded, there are still unsolved problems: mass gap, quantization of gravity, grand unified theories, neutrino masses, dark matter, etc. To reveal physics beyond the standard model, many researchers have addressed these problems.

Symmetry is essential in a gauge theory and several types of symmetry play important roles in modern physics to construct theories. This can not be overemphasized. It is considered that a theory with a higher symmetry was realized in the early universe and the symmetry of the theory spontaneously breaks down to the theory indicated by $\mathrm{SU}(3)_c \times \mathrm{SU}(2)_L \times \mathrm{U}(1)_Y$ and the other types of symmetry through the time evolution of the universe. In other words, it is expected that, just as a state of water changes between gas, liquid and solid, phase transitions associated with spontaneous symmetry breaking occurred in the universe during the evolution of the spacetime. Spontaneous symmetry breaking is also a key concept in modern physics. Inspired by the Bardeen–Cooper–Schrieffer theory [1] on superconductivity, Y. Nambu and G. Jona-Lasinio introduced the concept to particle physics with chiral symmetry in 1961 [2,3]. In this thesis, we focus on a phase transition with chiral symmetry.

The chiral symmetry is related to the strong interactions. As is known that the strong interactions between quarks and gluons are described by quantum chromodynamics (QCD), a non-Abelian gauge theory in quantum field theories. Asymptotic freedom is a property of QCD [4,5]. At a high energy scale, perturbative approaches that work in quantum electrodynamics are valid even in QCD. However, at a low energy scale, perturbative approaches do not work and a non-trivial vacuum structure, called the QCD vacuum, appears. In the non-trivial vacuum, color confinement and chiral symmetry breaking occur: the former is a phenomenon

that quarks and gluons are not observed in isolation and the latter a mechanism that hadrons dynamically obtain their mass through the condensates of quarks and anti-quarks. To investigate the vacuum structure, several approaches has been attempted: numerical calculations by using lattice QCD (LQCD) that is a part of lattice gauge theories and effective models that are induced by approximations and phenomenological considerations. Because LQCD is constructed on a discretized Euclidean spacetime, a path integral becomes finite-dimensional and hence can run on computers from the first principles. The effective models are not the genuine QCD, but they can be discussed on a continuous spacetime and calculated exactly. Moreover, the effective models can also have theoretically rich structures, such as integrability.

Phase transitions are phenomena that appear at several scales, as in particle physics and condensed matter physics. Revealing a phase structure of a target is often a research goal in several fields in physics, of course, QCD. For example, the schematic QCD phase diagram is shown in Fig. 1.1: the vertical axis denotes temperature of the system and the horizontal axis denotes quark chemical potential which is a conjugate variable of quark number density. The chiral symmetry is broken in the hadron phase at a low temperature and a low chemical potential, and restored in the other phase. It is an approximate symmetry, but this is a clue to investigate the phase structure.

As is mentioned above, LQCD is a powerful non-perturbative tool to analyze the low energy region, but there is the notorious problem called the sign problem at a finite quark chemical potential [6,7]. The problem is caused by failure to interpret an integrand at a finite chemical potential as a probability in the Monte Carlo method. Integrating degree of freedom of quarks with a finite chemical potential, μ, one obtains a path integral measure, $M(\mu)$ that satisfies $(M(\mu))^* = M(-\mu^*)$. This problem is common in particle physics and condensed matter physics as long as the Monte Carlo method is employed. To resolve the problem, some approaches are proposed: the Taylor expansion [8, 9], the analytic continuation from imaginary chemical potential [10–14], the complex Langevin method [15–19], the Lifschetz thimble method [20, 21], and the tensor renormalization group [22–25]. The tensor renormalization group is particularly a method that has been developed in condensed matter physics. Since the area that can be analyzed by these approaches are still restricted, the bulk of the QCD phase diagram has been illustrated by using the effective models. As the other approach close to the effective model, two-color QCD is proposed. In this theory, there is no sign problem. The two-color QCD is different from the QCD in terms of symmetry, but it is reported that the theory describes quantitatively three-color QCD [26]. Furthermore, the effective models play important roles at present.

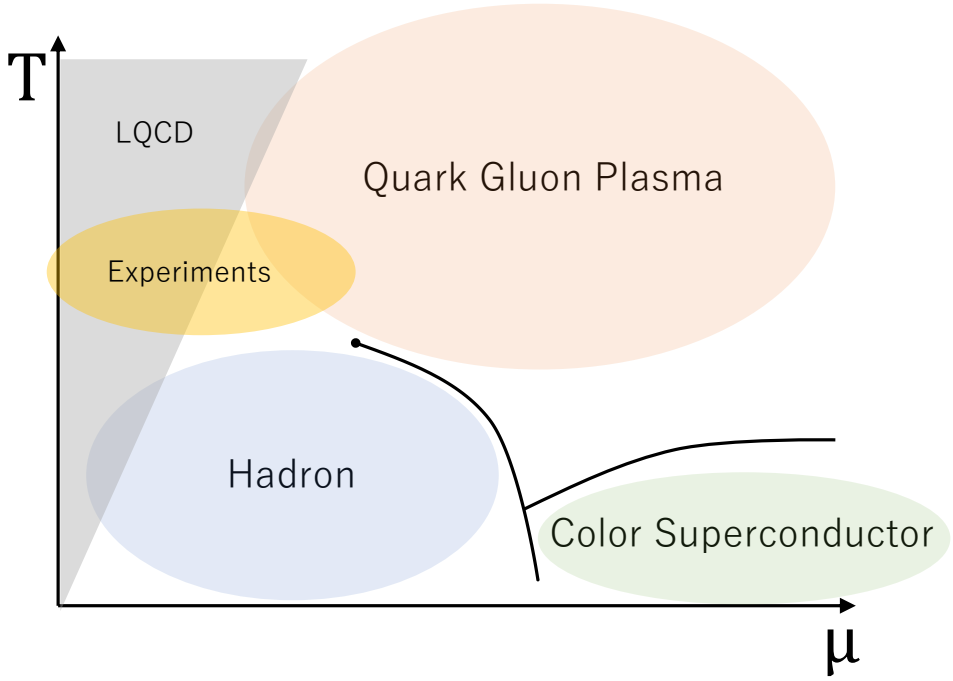

Fig. 1.1: Schematic QCD phase diagram.

There are various effective models to investigate the phase structure. The Nambu–Jona-Lasinio (NJL) model [2,3] is a simple model that describes dynamical chiral symmetry breaking via quark and anti-quark interactions, and is often used for the purpose in terms of chiral symmetry [27, 28]. Some types of four-fermion interaction models exist: the Gross–Neveu model [29] that has a discretized symmetry through a quark and anti-quark interaction, the extended NJL models with diquarks [30, 31], and the Polyakov-loop extended NJL model [32] that includes the effects of the color confinement. We adopt a four-fermion interaction model, mainly the Gross–Neveu model, to analyze and discuss the phase structure with the chiral symmetry, in this thesis.

States of matter depend on the physical conditions of surrounding systems. In Fig. 1.1, the state of matter is designated by temperature and quark chemical potential. There are, of course, various parameters to specify the condition of the system: temperature, entropy, pressure, volume of the system, particle number, chemical potential, curvature of the spacetime, magnetic field, rotational velocity, boundary conditions, topology, dimensions of the spacetime, and so on. A phase is basically realized by a state with the lowest thermodynamic potential under the parameters considered in the system. Thus, studying with parameters in addition to temperature and chemical potential leads to a better understanding of phase structures. By using four-fermion interaction models, phase transitions in various conditions are researched [27, 28, 33–35].

Related to high-energy experiments and compact stars (e.g. neutron stars), effects from the magnetic field [36] and the rotational velocity [37, 38] to the phase structure are interesting

to many researchers. The characteristic points of the two conditions are respectively the dimensional reduction [39, 40] that is a phenomenon in which an effective dimension becomes lower than the original dimension, D, such as $D \to D - 2$, and finite-volume effects with topology of boundaries [41]. Moreover, although LQCD contains artifacts, finite-volume effects and topological contributions from boundaries are not negligible in condensed matter physics and LQCD. Looking back at the early universe, all the matter might be confined inside an extremely small size space with a non-trivial topology. In string theory, the existence of compactified extra dimensions is predicted. Thus, we believe that it is significant to reconsider the finite-size effects, the contributions from the boundaries, and low-dimensional physics. In this thesis, we discuss not only the thermal effects but also the finite-size effects and the contributions from the boundaries on the phase structure for the chiral symmetry by using the four-fermion interaction model.

There are some works studying the finite-size effect on the chiral symmetry in four-fermion interaction models. Periodic and anti-periodic boundary conditions are often imposed [42–46] (Refs. [47, 48] are in LQCD). It is found that the chiral symmetry breaking tends to be enhanced because of the finite-size effect for the periodic boundary condition. On the contrary, it is observed that the anti-periodic boundary condition tends to restore the chiral symmetry. In this context, the finite temperature and chemical potential in the Matsubara formalism can be regarded as the size and boundary condition for the imaginary time direction. The boundary conditions can be more generalized to a U(1)-valued boundary condition for a compactified space, such as the one-dimensional sphere $\mathbb{S}^1$. Some works on the U(1)-valued boundary condition have previously done [49–54]. In general, such a boundary condition is introduced from the Aharonov–Bohm effect [55] in an Abelian gauge theory. For instance, the finite-size effect with the U(1)-valued boundary condition can be realized by the presence of magnetic flux in a ring or cylinder. In condensed matter physics, inhomogeneous condensates are discussed in a superconducting ring with magnetic flux [54]. As is discussed in [56] for high energy physics, it is also pointed out that inhomogeneous phases can be favored in a finite-size system.

To clarify the physical picture, it is important to evaluate thermodynamic quantities in addition to the dynamically generated fermion mass; we calculate particle number density and pressure. A well-known finite-size effect in quantum systems is the Casimir effect [57–70] which is a phenomenon of attraction between two uncharged conductive plates placed parallel. This is understood to be a phenomenon caused by a non-trivial vacuum. The Casimir force was firstly introduced as an attractive force, but later it was pointed out that the force could also be repulsive [71–73]. There is a study to connect the attractive force with the repulsive force for perfect electromagnetic conductor plates [74]. These discussions are based on electromagnetic fields, in other words, bosonic and vector fields. The Casimir effect has been studied in a four-fermion interaction model [75–77]; particularly, the sign-flip phenomena is also found in Ref. [76]. In the context of lattice simulations, the Casimir effect has been

also studied [47, 48, 78–80].

In this thesis, we study the finite-size effect on chiral symmetry breaking in a strongly coupled system of fermions by using a four-fermion interaction model. To clarify the discussion, we consider a simple condition: one-dimensional sphere, $\mathbb{S}^1$, as a part of the background. Our purpose is to show the finite-size effect on phase diagrams and clarify the phenomenological consequences by evaluating the thermodynamic quantities.

This thesis is organized as follows: In Chapter 2, we give brief introductions about chiral symmetry breaking in four-fermion interaction models without finite-size effects. In this thesis, we evaluate the effective potential in the leading order of the $1/N$ expansion with supposing a homogeneous chiral condensate. Next, the model at a finite temperature and a finite chemical potential is introduced with a phase diagram in terms of the chiral symmetry. In Chapter 3, we show the finite-size effects on chiral symmetry breaking in the Gross–Neveu model at zero temperature based on [81]. We also improve the effective potential analysis from the previous work [50]. Behavior of the dynamically generated fermion mass affected by the finite-size effects is shown. We discuss the stable size with the Casimir effect. In Chapter 4, chiral symmetry breaking at a finite temperature and a finite chemical potential is discussed with the finite-size effects based on [82]. To investigate the precise phase structure, we introduce new symbols and show the structure on bifurcation diagrams. We discuss the phase structure and the stability of the system with thermodynamic quantities. Finally, Chapter 5 is devoted to the summary and discussions.

Chapter 2

Four-Fermion Interaction Model

In this chapter, we briefly review four-fermion interaction models: the Nambu–Jona-Lasinio (NJL) model [2,3] and the Gross–Neveu (GN) model [29]. Both the models are well-known as effective models of the quantum chromodynamics (QCD) in terms of the chiral symmetry and the asymptotic freedom. They are simple models that describe spontaneous chiral symmetry breaking. These two models are distinguished by the interaction terms and enjoy slightly different symmetries. Although this difference does not affect on our analysis, we will mention a note in two dimensions later.

2.1 Nambu–Jona-Lasinio Model

Let us consider an action of the NJL model with N_f-flavor fermions on a D-dimensional Minkowski spacetime, $\mathcal{M}^D$, $(2 \leq D < 4)$:

$$S_{\mathrm{NJL}} = \int \mathrm{d}^D x \left[\bar{\psi}(x) i\gamma^\mu \partial_\mu \psi(x) + \frac{\lambda_0}{2N_c} \left((\bar{\psi}(x)\psi(x))^2 + (\bar{\psi}(x) i\gamma_5 \tau^a \psi(x))^2 \right) \right], \tag{2.1}$$

where λ_0 denotes a coupling constant of the four-fermion interaction, N_c the number of the color, and τ^a a generator of $\mathrm{SU}(N_f)$ $(a = 1, 2, \ldots, N_f^2 - 1)$. λ_0 has the mass dimension $-(D-2)$. The indices of the flavors and colors are omitted below. Such a model is introduced by Y. Nambu and G. Jona-Lasinio as first in the papers [2,3]. The model is evaluated in four dimensions $(D = 4)$, and hence the coupling has the mass dimension -2. This action (2.1) is invariant under a global transformation of $\mathrm{U}(N_f)_L \times \mathrm{U}(N_f)_R$:

$$\psi_\chi \to e^{i\theta_\chi^a \tau^a + i\theta_\chi} \psi_\chi, \qquad (\theta_\chi^a, \theta_\chi \in \mathbb{R}) \tag{2.2}$$

where ψ_χ $(\chi = L, R)$ denote left- and right-handed fermions, respectively. In particular, we are interested in $\mathrm{U}(1)_A$, a part of the group. A transformation of the group is called a chiral transformation:

$$\psi(x) \to e^{i\gamma_5 \theta} \psi(x), \qquad (\theta \in \mathbb{R}). \tag{2.3}$$

The invariance under the chiral transformation is due to no mass term.

A generating functional of the NJL model is given by

$$Z_{\mathrm{NJL}} = \int \mathcal{D}\psi\, \mathcal{D}\bar{\psi}\, e^{iS_{\mathrm{NJL}}}. \tag{2.4}$$

Inserting a constant that is expressed as a path integral of auxiliary fields, $\hat{\sigma}(x)$ and $\hat{\pi}^a(x)$,

$$\int \mathcal{D}\hat{\sigma}\, \mathcal{D}\hat{\pi}^a \exp\left[-i\frac{N_c}{2\lambda_0}\int \mathrm{d}^D x\, \left(\hat{\sigma}(x)^2 + \hat{\pi}^a(x)^2\right)\right], \tag{2.5}$$

into the generating functional (2.4), and using the invariance of a path integral measure under shifts, we obtain

$$Z_{\mathrm{NJL}} = \int \mathcal{D}\psi\, \mathcal{D}\bar{\psi}\, \mathcal{D}\hat{\sigma}\, \mathcal{D}\hat{\pi}^a\, e^{iS_{a\mathrm{NJL}}}, \tag{2.6}$$

$$S_{a\mathrm{NJL}} = \int \mathrm{d}^D x\, \left[\bar{\psi}(x)\left(i\gamma^\mu\partial_\mu - \hat{\sigma}(x) - i\gamma_5\tau^a\hat{\pi}^a(x)\right)\psi(x) - \frac{N_c}{2\lambda_0}\left(\hat{\sigma}(x)^2 + \hat{\pi}^a(x)^2\right)\right]. \tag{2.7}$$

The Euler–Lagrange equation for $\hat{\sigma}(x)$ and $\hat{\pi}^a(x)$ gives us constraints, $\hat{\sigma}(x) = -\lambda_0\bar{\psi}(x)\psi(x)/N_c$ and $\hat{\pi}^a(x) = -\lambda_0\bar{\psi}(x)i\gamma_5\tau^a\psi(x)/N_c$, respectively. Substituting these into the action (2.7), the original one (2.1) is reproduced. At the classical level, the auxiliary fields are proportional to composite operators of a fermion and an anti-fermion. Thus, the finite vacuum expectation value of the auxiliary fields indicates spontaneous symmetry breaking of the chiral symmetry.

The action (2.7) is written as quadratic forms of the fermions and auxiliary fields. Integrating out the fermion and anti-fermion, the generating functional and the action are rewritten as

$$Z_{\mathrm{NJL}} = \int \mathcal{D}\hat{\sigma}\, \mathcal{D}\hat{\pi}^a\, e^{iN_c S[\hat{\sigma},\hat{\pi}^a]}, \tag{2.8}$$

$$S[\hat{\sigma},\hat{\pi}^a] = -\frac{1}{2\lambda_0}\int \mathrm{d}^D x\, \left(\hat{\sigma}(x)^2 + \hat{\pi}^a(x)^2\right) - i\ln\mathrm{Det}\left[i\gamma^\mu\partial_\mu - \hat{\sigma}(x) - i\gamma_5\tau^a\hat{\pi}^a(x)\right], \tag{2.9}$$

with Det denoting the determinant over the flavor indices, the spinor indices, and the continuous spacetime coordinates. This generating functional (2.8) (or this action (2.9)) is represented only by the degrees of freedom of the auxiliary fields. The above manner that makes a four-fermion interaction term into a quadratic form by introducing a (pseudo)scalar field, is called the Hubbard–Stratonovich transformation [83, 84], or the auxiliary field method [85].

Although there is no degree of freedom of the fermion in the generating functional (2.8), it is still difficult to evaluate analytically the action (2.9). To resolve this problem, we apply the $1/N_c$ expansion and assume a homogeneous chiral condensate, in other words the vacuum expectation values of $\hat{\sigma}(x)$ and $\hat{\pi}(x)$ are independent of the temporal and spatial coordinates. We separate the auxiliary fields into the vacuum expectation values and fluctuations,

$$\hat{\sigma}(x) = \sigma(x) + \tilde{\sigma}(x), \qquad \hat{\pi}^a(x) = \pi^a(x) + \tilde{\pi}^a(x). \tag{2.10}$$

$\sigma(x)$ denotes an order parameter of chiral symmetry. Under the $1/N_c$ expansion, we obtain the effective action,

$$\Gamma[\sigma,\pi^a] = -i\ln Z_{\mathrm{NJL}} = N_c\left(S[\sigma,\pi^a] + O\left(1/N_c\right)\right). \tag{2.11}$$

Assuming the homogeneous chiral condensate, $\sigma(x) = \sigma$ and $\pi^a(x) = \pi^a$, we obtain the effective potential in the leading order of the $1/N_c$ expansion,

$$V(\sigma, \pi^a) = -\frac{S[\sigma, \pi^a]}{\int \mathrm{d}^D x} = \frac{\sigma^2 + (\pi^a)^2}{2\lambda_0} - \frac{N_f \,\mathrm{tr}\, I}{2} \int \frac{\mathrm{d}^D k}{i(2\pi)^D} \ln\left(-k^2 + \sigma^2 + (\pi^a)^2\right), \tag{2.12}$$

where the trace, tr, denotes the diagonal sum with respect to the spinor indices. In our numerical calculations, we set $\mathrm{tr}\, I = 2^{D/2}$. A vacuum state (equivalently, a ground state) is determined by the minimum of the effective potential in the parameter space of σ and π^a. The value of the effective potential does not change as long as $\sigma^2 + (\pi^a)^2$ has the same value. Therefore, if $\sigma^2 + (\pi^a)^2 \neq 0$, the vacuum states distinguished by the values of σ and π^a are infinitely degenerated. Because these states are equivalent, we can choose the vacuum state satisfying $\pi^a = 0$ without loss of generality ($V(\sigma) = V(\sigma, \pi^a = 0)$). In addition, we normalize the effective potential at $\sigma = 0$ to $V(0) = 0$.

The effective potential (2.12) contains an UV divergence. It is known that results produced by the NJL model depend on regularization schemes because the model is not renormalizable [86, 87] as indicated by the mass dimension of the coupling, -2, in four dimensions. Here, we show some regularization schemes: the sharp cutoff regularizations, and the dimensional regularization.

Three-momentum cutoff regularization

First, we introduce a three-momentum cutoff parameter Λ_3 in $D = 4$ as

$$\int \frac{\mathrm{d}^4 k}{i(2\pi)^4} \to \int \frac{\mathrm{d}k^0}{i2\pi} \int_{\boldsymbol{k}^2 \leq \Lambda_3^2} \frac{\mathrm{d}^3 \boldsymbol{k}}{(2\pi)^3}, \tag{2.13}$$

then the effective potential is given by

$$V_{\Lambda_3}(\sigma) = \frac{\sigma^2}{2\lambda_0} - \frac{N_f}{8\pi^2} \left(\Lambda_3 \left(2\Lambda_3^2 + \sigma^2\right) \sqrt{\Lambda_3^2 + \sigma^2} + \frac{\sigma^4}{2} \ln\left(\frac{\sigma^2}{(\Lambda_3 + \sqrt{\Lambda_3^2 + \sigma^2})^2} \right) \right) + \frac{N_f \Lambda_3^4}{4\pi^2}. \tag{2.14}$$

Four-momentum cutoff regularization

In a similar way, we can also introduce a four-momentum cutoff parameter Λ_4 in $D = 4$ after the Wick rotation as

$$\int \frac{\mathrm{d}^4 k}{i(2\pi)^4} f(-k^2) \to \int_{\boldsymbol{k}^2 \leq \Lambda_4^2} \frac{\mathrm{d}^4 \boldsymbol{k}}{(2\pi)^4} f(\boldsymbol{k}^2), \tag{2.15}$$

where f is an arbitrary analytic function. The effective potential is give by

$$V_{\Lambda_4}(\sigma) = \frac{\sigma^2}{2\lambda_0} - \frac{N_f}{16\pi^2} \left(\Lambda_4^4 \ln\left(1 + \frac{\sigma^2}{\Lambda_4^2}\right) - \sigma^4 \ln\left(1 + \frac{\Lambda_4^2}{\sigma^2}\right) + \sigma^2 \Lambda_4^2 \right). \tag{2.16}$$

Proper-time regularization

Another regularization scheme that uses a sharp cutoff is the proper-time method [88, 89]. It is useful to keep in mind the formal identity for a operator $\mathcal{O}$, related to the zeta function regularization [90, 91],

$$\operatorname{tr}\ln\mathcal{O} = -\lim_{s\to 0}\frac{\mathrm{d}}{\mathrm{d}s}\frac{1}{\Gamma(s)}\operatorname{tr}\int_0^\infty \mathrm{d}\tau\,\tau^{s-1}e^{-\tau\mathcal{O}}. \tag{2.17}$$

To treat the divergent term, we introduce a regularization parameter Λ_{pt} as

$$\int\frac{\mathrm{d}^4k}{i(2\pi)^4}\ln\left(-k^2+\sigma^2\right) \to -\int_{1/\Lambda_{\mathrm{pt}}^2}^\infty \mathrm{d}\tau\,\tau^{-1}\int\frac{\mathrm{d}^4\boldsymbol{k}}{(2\pi)^4}e^{-\tau\left(\boldsymbol{k}^2+\sigma^2\right)}. \tag{2.18}$$

The effective potential in the proper-time method reads

$$V_{\mathrm{pt}}(\sigma) = \frac{\sigma^2}{2\lambda_0} + \frac{N_f}{8\pi^2}\int_{1/\Lambda_{\mathrm{pt}}^2}^\infty \mathrm{d}\tau\,\tau^{-3}e^{-\tau\sigma^2} - \frac{N_f\Lambda_{\mathrm{pt}}^4}{16\pi^2}. \tag{2.19}$$

In this method, the effective potential is written as an integral over a proper-time space with a lower limit, not as an integral over a momentum space with a upper limit.

Dimensional regularization

Finally, we introduce the dimensional regularization that is one of regularization schemes by using analytic continuation. Considering a complex number $D \neq 4$ (in particular, considering $2 \leq D < 4$), we can perform the integral over a momentum space,

$$\frac{1}{2}\int\frac{\mathrm{d}^Dk}{i(2\pi)^D}\ln\left(-k^2+\sigma^2\right) = \frac{\Gamma\left(1-\frac{D}{2}\right)}{(4\pi)^{D/2}}\frac{(\sigma^2)^{D/2}}{D}. \tag{2.20}$$

Thus, we obtain the effective potential,

$$V_{\mathrm{DR}}(\sigma) = \frac{\sigma^2}{2\lambda_0} - N_fC_D\frac{(\sigma^2)^{D/2}}{D}, \tag{2.21}$$

with a constant depending on the dimension D,

$$C_D = \frac{\operatorname{tr} I}{(4\pi)^{D/2}}\Gamma\left(1-\frac{D}{2}\right). \tag{2.22}$$

This term diverges in two and four dimensions. There is no scale parameter in this expression (2.21). We renormalize the coupling λ_0 with a renormalization scale, μ_r. The renormalization condition is given by

$$\left.\frac{\partial^2V_{\mathrm{DR}}(\sigma)}{\partial\sigma^2}\right|_{\sigma=\mu_r} = \frac{\mu_r^{D-2}}{\lambda_r}, \tag{2.23}$$

where λ_r indicates a renormalized coupling that has the mass dimension zero. The renormalized effective potential with the dimensional regularization is

$$V_{\mathrm{DR}}(\sigma) = \frac{1}{2}\left(\frac{1}{\lambda_r} + (D-1)N_fC_D\right)\sigma^2\mu_r^{D-2} - N_fC_D\frac{(\sigma^2)^{D/2}}{D}. \tag{2.24}$$

This expression is finite at $2 \leq D < 4$.

The NJL model at $D = 2$ is also called the chiral Gross–Neveu model. In particular, this model is renormalizable (The mass dimension of the coupling becomes zero in two dimensions.) and shares some features with the four-dimensional theory because these dimensions of a background spacetime is even. Hence, the results produced by the model in two dimensions does not depend on regularization schemes. Because of the well-known no-go theorem stated by N. Mermin, H. Wagner, P. Hohenberg and S. Coleman [92–94], spontaneous chiral symmetry breaking is prohibited in two dimensions, but the theorem becomes invalid in the leading order of the $1/N_c$ expansion. This is because fluctuations that destroy the spontaneous symmetry breaking, are suppressed in the next to leading order of the expansion (see Eq. (2.11)).

We comment on the dimensional regularization in the NJL model. Targets which is analyzed by using this model is usually in four dimensions, but one can not take the four-dimensional limit in this regularization because of the non-renormalizability. As is discussed in Refs. [95–98], the results from the dimensional regularization in $2 < D < 2.5$ is similar to the results from the sharp cutoff; some properties of the nonet meson are reproduced.

As examples, we show the behavior of the effective potential for comparison of the different cutoff regularizations in Figs. 2.1 and 2.2 ($N_f = 1$). It can be seen that there is only one minimum of the effective potential at the origin, $\sigma = 0$, for the coupling constant smaller than a certain value, but when the coupling constant becomes larger than the value, the minimum is located at a point that is not the origin, $\sigma \neq 0$. In other words, spontaneous chiral symmetry occurs for the coupling constant larger than a certain value, and then the fermion mass is dynamically generated. Such a value of the coupling constant at which a second-order phase transition between a chiral symmetric phase and a chiral broken phase occurs, is called a critical coupling constant.

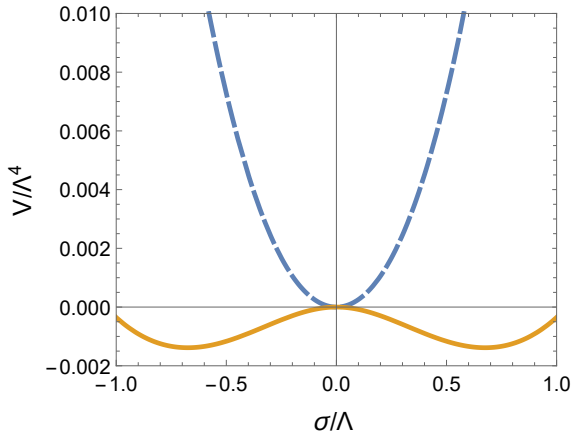

Fig. 2.1: The behavior of the effective potential: the three-momentum cutoff regularization. The coupling constant smaller than the critical one corresponds to the blue dashed curve ($\lambda_0\Lambda_3^2 = \pi^2$), and larger than the critical one the orange solid curve ($\lambda_0\Lambda_3^2 = 3\pi^2$).

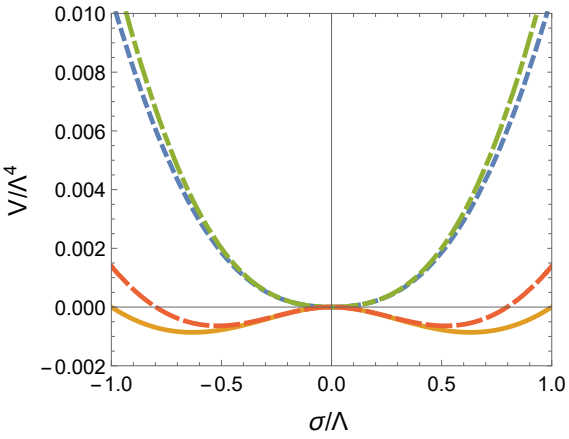

Fig. 2.2: The behavior of the effective potential: the four-momentum cutoff regularization/the proper-time regularization. In the both cases, the coupling constant smaller than the critical one corresponds the blue dotted/green dot-dashed curve ($\lambda_0\Lambda_{4/\mathrm{pt}}^2 = 3\pi^2$), and larger than the critical one the orange solid/red dashed curve ($\lambda_0\Lambda_{4/\mathrm{pt}}^2 = 8\pi^2$).

The minimum of the effective potential corresponds to a vacuum state that has the lowest energy. Therefore, to discuss spontaneous chiral symmetry breaking in the model, we need to find out the minimum. This is a solution of the gap equation,

$$\left.\frac{\partial V(\sigma)}{\partial\sigma}\right|_{\sigma=m} = 0, \tag{2.25}$$

with m denoting a dynamically generated fermion mass. The behavior of the generated fermion mass is shown in Fig. 2.3, and we can observe the second-order phase transitions. The value of the generated fermion mass monotonically increases as the coupling constant increases. Rewriting the gap equation as

$$0 = \left.\frac{\partial V(\sigma)}{\partial\sigma}\right|_{\sigma=m} = mf(m;\lambda_0), \tag{2.26}$$

where $f(m;\lambda_0)$ is a function of zero or more orders of m, and taking the chiral limit, $m \to 0$, we obtain a critical coupling λ_c from $f(m;\lambda_c) = 0$. From Eq. (2.13), (2.15), and (2.19), the critical coupling constant is $\lambda_{3,c}\Lambda_3^2 = 2\pi^2/N_f$ in the three-momentum cutoff regularization, and $\lambda_{4,c}\Lambda_4^2 = \lambda_{\mathrm{pt},c}\Lambda_{\mathrm{pt}}^2 = 4\pi^2/N_f$ in the four-momentum cutoff and proper-time regularizations.

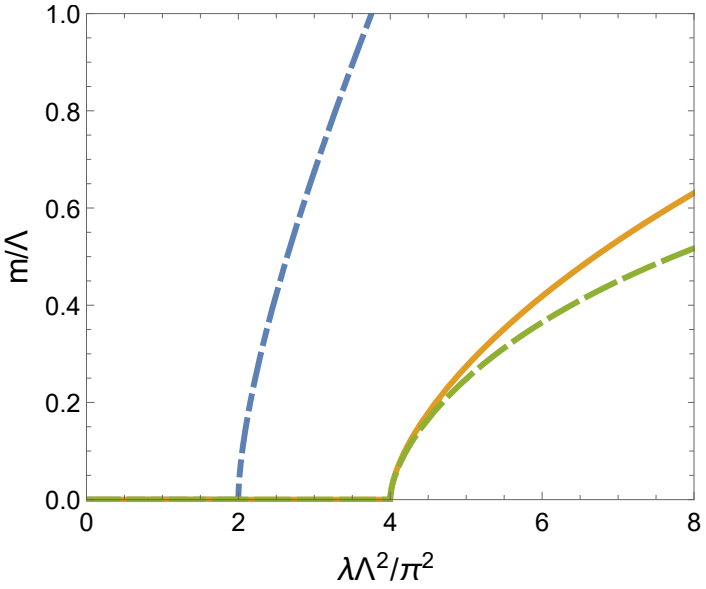

Fig. 2.3: The dynamically generated fermion mass as a function of the coupling constant, $\lambda_0 \Lambda_{3/4/\mathrm{pt}}^2/\pi^2$ ($N_f = 1$). The blue dot-dashed curve corresponds to the three-momentum cutoff regularization, the orange solid curve the four-momentum cutoff regularization, and the green dashed curve the proper-time regularization.

2.2 Gross–Neveu Model

The GN model is a four-fermion interaction model similar to the NJL model. The action on a D-dimensional Minkowski spacetime, $\mathcal{M}^D$, ($2 \leq D < 4$) reads

$$S_{\mathrm{GN}} = \int \mathrm{d}^D x \left[\bar{\psi}(x) i\gamma^\mu \partial_\mu \psi(x) + \frac{\lambda_0}{2N} (\bar{\psi}(x)\psi(x))^2 \right], \tag{2.27}$$

with λ_0 denoting a coupling constant of a four-fermion interaction that has the mass dimension $-(D-2)$, and N the number of copies of fermions. This action (2.27) is invariant under a discrete chiral ($\mathbb{Z}_2$) transformation, $\psi(x) \to \gamma_5 \psi(x)$. The action, of course, has the symmetry, $\psi \to -\psi$. In the original paper [29], the model is constructed in two dimensions, and thus the coupling has no mass dimension.

Applying the same manner with the NJL model, we can obtain the effective potential of the GN model in the leading order of the $1/N$ expansion,

$$V(\sigma) = \frac{1}{2} \left(\frac{1}{\lambda_r} + (D-1) C_D \right) \sigma^2 \mu_r^{D-2} - C_D \frac{(\sigma^2)^{D/2}}{D}, \tag{2.28}$$

where the coupling is renormalized according to the same procedure (2.23). We have used the dimensional regularization. Due to the discrete symmetry, the same expression as in Eq. (2.24), except for N_f, is obtained without choosing a vacuum state. And also, because of the same reason, spontaneous discrete chiral symmetry breaking is not forbidden in two

dimensions. Therefore, we employ the GN model to discuss spontaneous chiral symmetry breaking in two dimensions. The expression of the effective potential in two dimensions is

$$V(\sigma) = \frac{\sigma^2}{2\lambda_r} + \frac{\sigma^2}{4\pi}\left(-3 + \ln\left(\frac{\sigma}{\mu_r}\right)^2\right). \tag{2.29}$$

As mentioned above, the GN model in two dimensions is independent of regularization schemes due to its renormalizablity. Furthermore, the model in three dimensions, or in any dimension $2 \leq D < 4$, is renormalizable in the sense of the leading order of the $1/N$ expansion [99, 100]. In Fig. 2.4, the generated fermion mass in two and three dimensions are shown as a function of the renormalized coupling, and the latter exhibits the second-order phase transition. The chiral symmetry is always broken except for $\lambda_r = 0$ in two dimensions. The explicit expression of the generated fermion mass is obtained as

$$m = \mu_r \left(\frac{1}{\lambda_r C_D} + D - 1\right)^{\frac{1}{D-2}}. \tag{2.30}$$

And also, the critical coupling, $\lambda_{c,D}$, is given by

$$\lambda_{c,D} = -\frac{1}{C_D(D-1)}. \tag{2.31}$$

The behavior of the critical coupling is plotted in Fig. 2.5. For instance, $\lambda_{c,D=2} = 0$ and $\lambda_{c,D=3} = \pi/\sqrt{2} \simeq 2.22$. On the boundary, the second-order phase transition takes place.

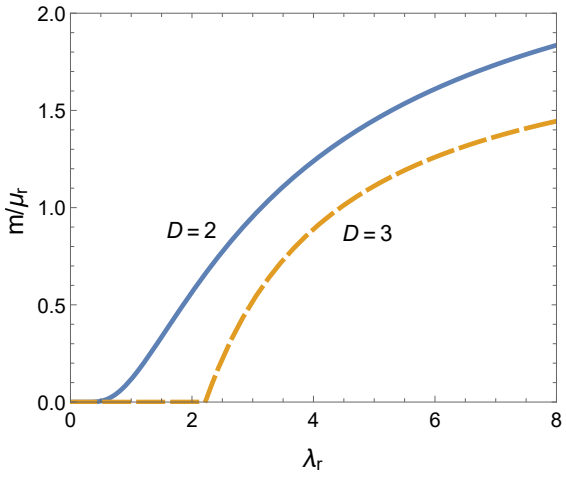

Fig. 2.4: The dynamically generated fermion mass as a function of the coupling constant in two (the blue solid curve) and three (the orange dashed curve) dimensions.

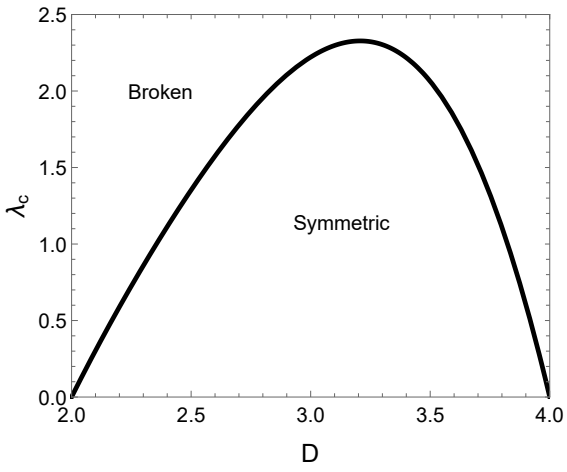

Fig. 2.5: The critical coupling as a function of the dimension, D. The chiral symmetry is restored in the area below the black curve, and broken in the other area.

As is shown by no mass dimension of the coupling, the GN model is renormalizable in two dimensions, and hence there is no regularization dependence. However, differences resulting from regularization schemes can also appear in two dimensions before one applies an

appropriate renormalization. We here compare the effective potentials derived from the cutoff regularization and the dimensional regularization in two dimensions. We can easily obtain the expression for a momentum cutoff regularization by replacing three with one in Eq. (2.13),

$$\begin{aligned} V_{\Lambda_1}(\sigma) &= \frac{\sigma^2}{2\lambda_0} - \int_{k^2 \le \Lambda_1^2} \frac{\mathrm{d}k}{2\pi} \sqrt{k^2+\sigma^2} \\ &= \frac{\sigma^2}{2\lambda_0} - \frac{1}{2\pi}\left(\Lambda_1^2 \sqrt{\Lambda_1^2+\sigma^2} + \frac{\sigma^2}{2} \ln \left(\frac{\left(\Lambda_1 + \sqrt{\Lambda_1^2+\sigma^2}\right)^2}{\sigma^2} \right) \right), \end{aligned} \tag{2.32}$$

with Λ_1 denoting the cutoff in two dimensions. Expanding this in powers of σ/Λ_1, we have

$$\frac{V_{\Lambda_1}(\sigma)}{\Lambda_1^2} = \frac{\sigma^2}{2\lambda_0\Lambda_1^2} + \frac{1}{4\pi}\left(\frac{\sigma}{\Lambda_1}\right)^2 \left(-1 - \ln 4 + \ln\left(\frac{\sigma}{\Lambda_1}\right)^2 \right) + O\left(\frac{\sigma^3}{\Lambda_1^3}\right), \tag{2.33}$$

that is shifted as $V_{\Lambda_1}(\sigma = 0) = 0$. The effective potentials (2.33) and (2.29) that is derived from the dimensional regularization are obviously distinguished in terms of the higher order terms of Λ_1, but also in terms of the coefficients in the second order.

Next, we briefly review the asymptotic freedom. The scale dependence of the renormalized coupling, λ_r, is determined by the renormalization group equation,

$$\mu_r \frac{\mathrm{d}V(\sigma)}{\mathrm{d}\mu_r} = 0, \tag{2.34}$$

in the leading order of the $1/N$ expansion. This equation based on the fact that physical quantities are explicitly independent of the renormalization scale, μ_r, which is artificially introduced. This equation is rewritten as

$$\mu_r \frac{\partial V(\sigma;\lambda_r,\mu_r)}{\partial \mu_r} + \beta(\lambda_r)\frac{\partial V(\sigma;\lambda_r,\mu_r)}{\partial \lambda_r} = 0, \tag{2.35}$$

where $\beta(\lambda_r)$ is a beta function that stands for a dependence of the coupling on μ_r, and the parameter dependence of the effective potential is written explicitly. Note that there is no renormalization of σ in the leading order of the $1/N$ expansion because of our definition of the auxiliary field, $\hat{\sigma}(x) \sim \lambda_0 \bar{\psi}(x)\psi(x)$ (below Eq. (2.7) at the page 7). Solving the equation (2.35), we obtain

$$\beta(\lambda_r) = \frac{D-2}{\lambda_{c,D}}(\lambda_{c,D} - \lambda_r)\lambda_r, \tag{2.36}$$

in the leading order of the $1/N$ expansion. This result is consistent with Ref. [34].

The behavior of the beta function is plotted in Fig. 2.6. In two dimensions, the beta function is always negative for $\lambda_r > 0$ (It means that the renormalized coupling is a monotonically decreasing function of μ_r.), and thus the theory is asymptotically free. On the other hand, there is an UV fixed point at $\lambda_r = \lambda_{c,D=3}$ in the three-dimensional theory; with increasing μ_r, the value of the coupling monotonically decreases for $\lambda_r > \lambda_{c,D=3}$, and increases for $\lambda_r < \lambda_{c,D=3}$.

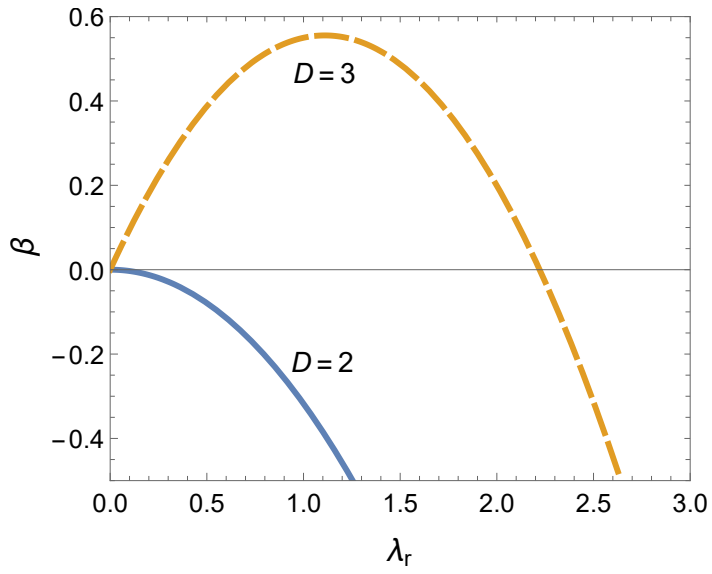

Fig. 2.6: The beta function as a function of the coupling in two (the blue solid curve) and three (the orange dashed curve) dimensions.

To make clear the behavior of the renormalized coupling, we solve a differential equation,

$$\frac{\mathrm{d}\lambda_r}{\mathrm{d}t} = \beta(\lambda_r) = \frac{D-2}{\lambda_{c,D}}(\lambda_{c,D} - \lambda_r)\lambda_r, \tag{2.37}$$

with a dimensionless parameter, $t = \ln(\mu_r/\mu_{r,0})$, and a reference scale, $\mu_{r,0}$. Given $\lambda_r(t = 0) = \lambda_{r,0}$ at $t = 0$ ($\mu_r = \mu_{r,0}$) as an initial condition, we obtain a running coupling constant,

$$\lambda_r(t) = \lambda_{c,D}\left(1 - \frac{\lambda_{r,0} - \lambda_{c,D}}{\lambda_{r,0}} e^{-(D-2)t}\right)^{-1}. \tag{2.38}$$

The behavior of the running coupling is shown in Fig. 2.7. The coupling constant for a strong coupling, $\lambda_{r,0} > \lambda_{c,D}$, monotonically decreases with increasing the renormalization scale, but for a weak coupling, $\lambda_{r,0} < \lambda_{c,D}$, shows the opposite behavior.

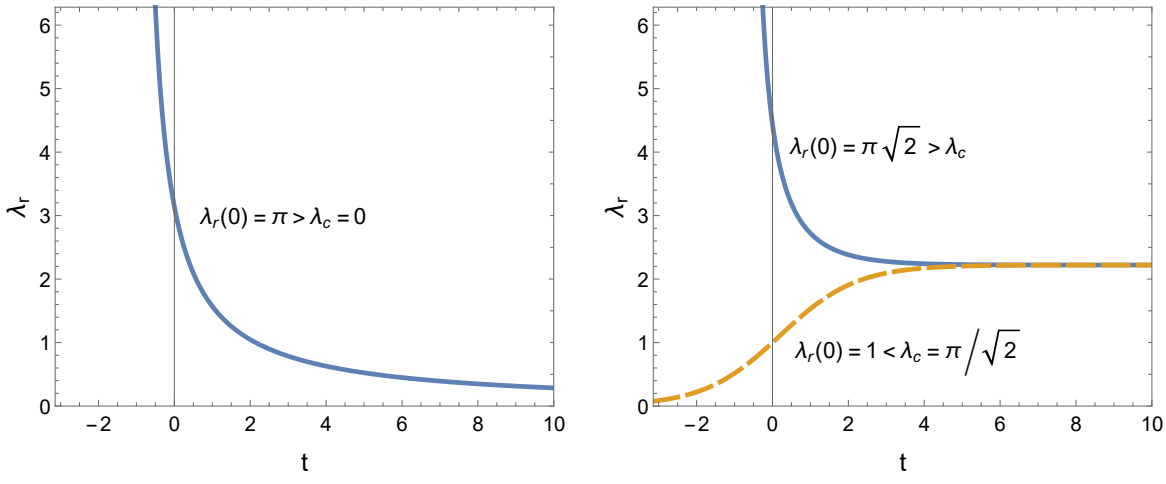

$D = 2$ $D = 3$

Fig. 2.7: The running coupling constant as a function of the dimensionless parameter, $t = \ln(\mu_r/\mu_{r,0})$ (left: two dimensions, and right: three dimensions). The blue solid curves indicate that the initial state is the strong coupling, $\lambda_{r,0} > \lambda_{c,D}$. The orange dashed curve indicates that the initial state is the weak coupling, $\lambda_{r,0} < \lambda_{c,D}$.

2.3 Massive Model

We have mentioned the no-go theorem for continuous symmetries in Chapter 2.1 in two dimensions, and also mentioned that the theorem becomes invalid in the leading order of the $1/N$ expansion. Alternatively, we can also avoid the theorem by choosing a discrete symmetry as the symmetry of the theory (Chapter 2.2).

In this section, we consider a massive model in four-fermion interaction models. For simplicity, we use the massive Gross–Neveu model,

$$S_{m\mathrm{GN}} = \int \mathrm{d}^D x \left[\bar{\psi}(x)\left(i\gamma^\mu\partial_\mu - m_{\mathrm{bare}}\right)\psi(x) + \frac{\lambda_0}{2N}(\bar{\psi}(x)\psi(x))^2\right], \tag{2.39}$$

with m_{bare} denoting a bare fermion mass. The other parameters are the same ones in the massless model (2.27). Because of the mass term that is a explicitly breaking , $m_{\mathrm{bare}}\bar{\psi}(x)\psi(x)$, the model does not enjoys the discrete chiral symmetry; in that sense, the discrete chiral symmetry becomes an approximate symmetry. The massive model is not only realistic, but also can avoid the no-go theorem. Thus, it is worthwhile to consider the massive model.

After shifting the auxiliary field by m_{bare}, we apply the same manner in the massless GN model, and then obtain the effective potential in the leading order of the $1/N$ expansion,

$$V(\sigma) = \frac{\sigma^2 - 2m_{\mathrm{bare}}\sigma}{2\lambda_0} - C_D\frac{(\sigma^2)^{D/2}}{D}, \tag{2.40}$$

where the constant term, $\lambda_0^{-1}m_{\mathrm{bare}}^2$, is omitted. Following the renormalization procedure

(2.23), the effective potential is rewritten as

$$V(\sigma) = \left(\frac{1}{\lambda_r} - C_D(D-1)\right)\left(\frac{\sigma^2}{2} - m_{\rm bare}\sigma\right)\mu_r^{D-2} - C_D\frac{(\sigma^2)^{D/2}}{D}. \tag{2.41}$$

Taking the two-dimensional limit, we can see that the effective potential contains a divergence proportional to the mass term. Hence, in order to construct the finite theory in $2 \leq D < 4$, we need to renormalize the divergence to the mass.

The physical mass is defined as a pole position of the propagator, and realized as the minimum of the effective potential [101, 102]. In that sense, $m_{\rm bare}$ itself does not imply physical mass unless it satisfies the minimum of the effective potential. In the weak coupling limit, $\lambda_r \to 0$, a mass parameter $m_{\rm bare}$ is dominant in determining the physical mass. When the mass parameter is zero, the effective potential is even and can have the minimum at $\sigma = 0$ for the weak coupling; intuitively, the mass parameter means the tilt of the effective potential.

Let us reconsider the massless model. The first-order derivative of the effective potential with respect to σ always satisfies zero at the origin, $\sigma = 0$. This implies the fact that there is always the trivial solution. Back to the massive theory again, the derivative at the origin satisfies,

$$\left.\frac{\partial V(\sigma)}{\partial\sigma}\right|_{\sigma=0} = -\left(\frac{1}{\lambda_r} + C_D(D-1)\right)m_{\rm bare}\mu_r^{D-2}. \tag{2.42}$$

This indicates that the gap equation in the massive theory, $m_{\rm bare} \neq 0$, does not always have the trivial solution, and also the tilt of the effective potential at the origin becomes divergent due to C_D in the two-dimensional limit.

To resolve this problem, we apply a renormalization condition to $m_{\rm bare}$ by using the derivative at the origin (2.42),

$$\left.\frac{\partial V(\sigma)}{\partial\sigma}\right|_{\sigma=0} = -\frac{m_r}{\lambda_r}\mu_r^{D-2}, \tag{2.43}$$

where m_r is a renormalized mass parameter. Under this condition, the divergence in the two-dimensional limit is removed, and the trivial solution is excluded as long as $m_r \neq 0$. The renormalized effective potential reads

$$V(\sigma) = \frac{1}{2}\left(\frac{1}{\lambda_r} + C_D(D-1)\right)\sigma^2\mu_r^{D-2} - \frac{m_r}{\lambda_r}\sigma\mu_r^{D-2} - C_D\frac{(\sigma^2)^{D/2}}{D}. \tag{2.44}$$

In the weak coupling limit, $\lambda_r \to 0$, the gap equation is approximately expressed as,

$$0 = \left.\frac{\partial V(\sigma)}{\partial\sigma}\right|_{\sigma=m} \simeq \frac{m - m_r}{\lambda_r}\mu_r^{D-2}, \tag{2.45}$$

then we can confirm the solution, $m = m_r$, being the minimum of the effective potential. Therefore, the renormalization condition for the mass parameter (2.43) means that the renormalized mass parameter gives a physical mass in the weak coupling limit. In Fig. 2.8, the behavior of the generated fermion mass is shown as a function of λ_r. We can observe that the

generated fermion mass monotonically and smoothly increases with increasing the coupling, and the chiral symmetry is not restored in the weak coupling limit, $\lambda_r \to 0$.

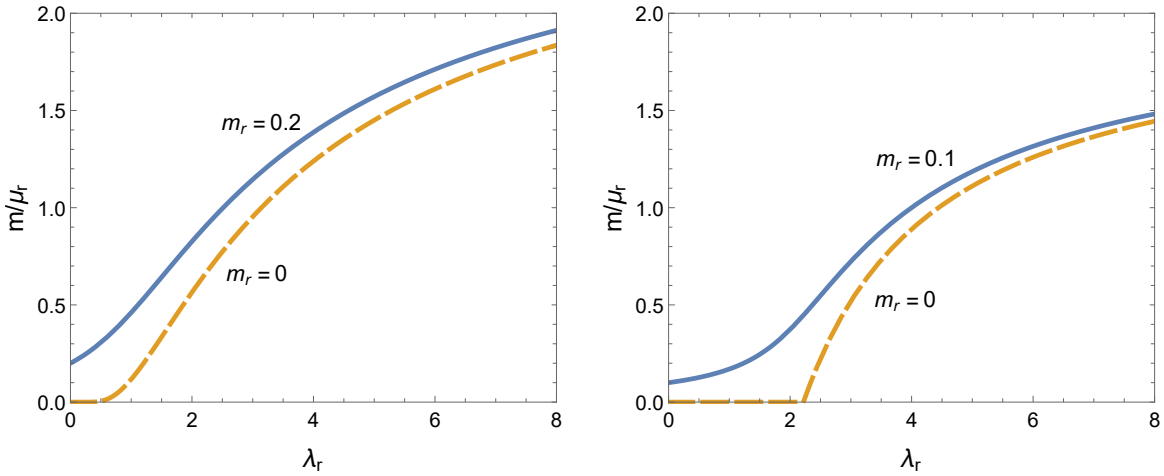

$D = 2$ $D = 3$

Fig. 2.8: The dynamically generated fermion mass as a function of λ_r (left: two dimensions, and right: three dimensions). The blue solid curve corresponds to the massive theory, and the orange dashed curve the massless theory.

Finally, we check the scale dependence of the mass parameter, m_r, in this section. In the massive model, the renormalization group equation (2.34) is written as

$$\mu_r \frac{\partial V(\sigma;\lambda_r,m_r,\mu_r)}{\partial \mu_r} + \beta(\lambda_r)\frac{\partial V(\sigma;\lambda_r,m_r,\mu_r)}{\partial \lambda_r} + m_r\gamma_m(\lambda_r)\frac{\partial V(\sigma;\lambda_r,m_r,\mu_r)}{\partial m_r} = 0, \tag{2.46}$$

where $\gamma_m(\lambda_r)$ is a coefficient related to the renormalized mass parameter, m_r. Solving this equation, the solution of $\beta(\lambda_r)$ is Eq. (2.36). The solution of $\gamma_m(\lambda_r)$ is given by

$$\gamma_m(\lambda_r) = -\frac{D-2}{\lambda_{c,D}}\lambda_r = \frac{\beta(\lambda_r)}{\lambda_{c,D}} - (D-2). \tag{2.47}$$

$\gamma_m(\lambda_r)$ is linear with respect to λ_r and monotonically decreases from $\gamma_m(\lambda_r = 0) = 0$ in arbitrary dimension.. Since we have solved $\beta(\lambda_r)$, we can also solve the differential equation,

$$\frac{\mathrm{d}\gamma_m(t)}{\mathrm{d}t} = -(D-2)\left(1 - \frac{\lambda_{r,0}-\lambda_{c,D}}{\lambda_{r,0}}e^{-(D-2)t}\right)^{-1} m_r, \tag{2.48}$$

then

$$m_r(t) = \frac{\lambda_{c,D}m_{r,0}}{\left(e^{(D-2)t}-1\right)\lambda_{r,0}+\lambda_{c,D}}, \tag{2.49}$$

with $m_r(t=0) = m_{r,0}$ at $t = 0$ as an initial condition. The behavior of the renormalized mass parameter, $m_r(t)$, is shown in Fig. 2.9. Regardless of whether the coupling is strongly or weakly coupled, the value of the mass parameter decreases as the renormalization scale increases.

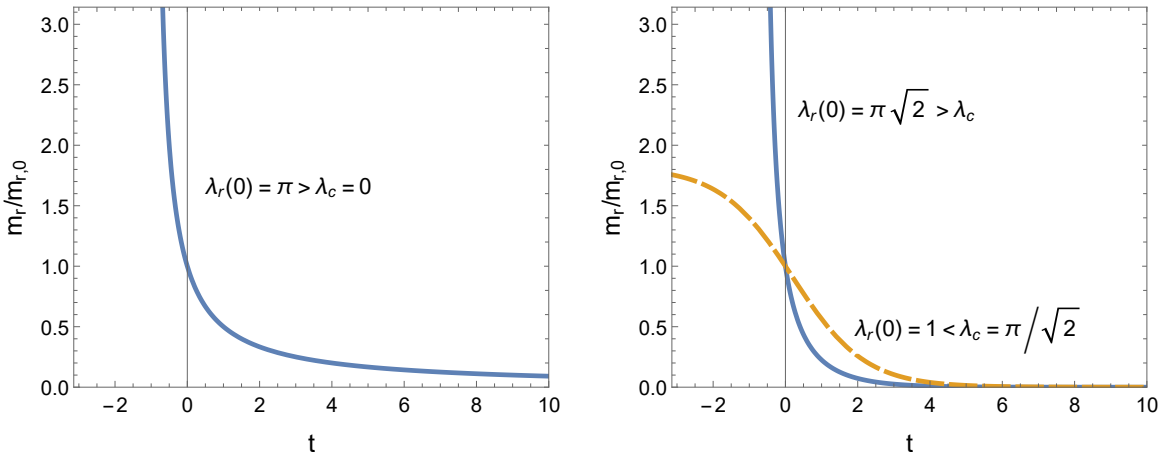

$D = 2$ $D = 3$

Fig. 2.9: The renormalized mass parameter as a function of $t = \ln(\mu_r/\mu_{r,0})$ (left: two dimensions, and right: three dimensions). The blue solid curves indicate that the initial state is the strong coupling, $\lambda_{r,0} > \lambda_{c,D}$, and the orange dashed curve indicates that the initial state is the weak coupling, $\lambda_{r,0} < \lambda_{c,D}$.

2.4 Finite Temperature and Chemical Potential

In order to deal with more realistic situations in four-fermion interaction models, we extend the models with a finite temperature and a finite chemical potential. Only thermal equilibrium systems are treated. In this section and the following chapters, we use basically the GN model, and the dimensional regularization.

The Matsubara formalism (or called the imaginary time formalism) [103–106] is well known as an extension method to a finite temperature systems. In this formalism, a time direction is extended to a complex plane by using analytic continuation, and a time, x^0, is replaced with an imaginary time, $x^0 \to x^D = -ix^0$ ($x^D \in \mathbb{R}$). The range of an integral over the imaginary time is limited to a finite interval, $[0, 1/T]$, for a temperature T. In fermion systems, an anti-periodic boundary condition is imposed to the imaginary time direction,

$$\psi(x^1, x^2, \ldots, x^D + 1/T) = -\psi(x^1, x^2, \ldots, x^D) \tag{2.50}$$

Thus, we can regard the imaginary time direction as a one-dimensional sphere, $\mathbb{S}^1$, with a circumference of $1/T$: the background spacetime $\mathbb{R}^{D-1} \times \mathbb{S}^1$. The generating functional (2.6) is replaced with a partition function in thermodynamics,

$$Z_{\mathrm{GN},T} = \int \mathcal{D}\psi\, \mathcal{D}\bar{\psi}\, e^{-S_{\mathrm{GN},T}}, \tag{2.51}$$

$$S_{\mathrm{GN},T} = \int \mathrm{d}^{D-1}x \int_0^{1/T} \mathrm{d}x^D \left[\bar{\psi}(x)\tilde{\gamma}^k \partial_k \psi(x) - \frac{\lambda_0}{2N}(\bar{\psi}(x)\psi(x))^2\right], \tag{2.52}$$

where $\tilde{\gamma}^k$ is a Euclidean gamma matrix, $(\tilde{\gamma}^k)^\dagger = -\tilde{\gamma}^k$. Because of the finite range of the integral, the Fourier transformation of fermions is discretized to the Matsubara frequencies, $\omega_n = (2n+1)\pi T$ $(n \in \mathbb{Z})$.

Next, we introduce a chemical potential, μ. According to the Noether's theorem, a particle number density is obtained as a conserved quantity from a global transformation, $\psi(x) \to e^{i\alpha}\psi(x)$ $(\alpha \in \mathbb{R})$: $\bar{\psi}(x)\gamma^0\psi(x)$. A chemical potential is a quantity that is conjugate to a particle number in thermodynamics. Hence, we can introduce a chemical potential into the thermal theory by replacing the action as follows,

$$S_{\mathrm{GN},T} \to S_{\mathrm{GN},T} + \mu \int \mathrm{d}^{D-1}x \int_0^{1/T} \mathrm{d}x^D \, \bar{\psi}(x)\gamma^D\psi(x). \tag{2.53}$$

Combining the discussions at a finite temperature and at a finite chemical potential, and applying the procedures described in Chapter 2.1 and 2.2, we obtain the effective potential in the leading order of the $1/N$ expansion,

$$V(\sigma;T,\mu) = \frac{\sigma^2}{2\lambda_0} - \frac{\operatorname{tr} I}{2} T \sum_{n=-\infty}^{\infty} \int \frac{\mathrm{d}^{D-1}\boldsymbol{k}}{(2\pi)^{D-1}} \ln\left(\boldsymbol{k}^2 + \tilde{\omega}_{\mu,n}^2 + \sigma^2\right), \tag{2.54}$$

with $\tilde{\omega}_{\mu,n} = \omega_n - i\mu$. The integral over in the continuous momentum space is replaced with the summation from $-\infty$ to ∞.

We perform the Matsubara sum. By using the useful identity related to the zeta function regularization (2.17), the second term in Eq. (2.54) can be written as

$$\lim_{s\to 0} \frac{\operatorname{tr} I}{2} \int \frac{\mathrm{d}^{D-1}\boldsymbol{k}}{(2\pi)^{D-1}} \frac{\mathrm{d}}{\mathrm{d}s} \frac{1}{\Gamma(s)} \int_0^\infty \mathrm{d}\tau \, \tau^{s-1} e^{-\tau(\boldsymbol{k}^2+\sigma^2)} T \sum_{n=-\infty}^{\infty} e^{-\tau\tilde{\omega}_{\mu,n}^2}. \tag{2.55}$$

After some calculations, we can confirm this term separated into terms come from the vacuum state (not thermal), and the Fermi–Dirac distribution in finite temperature systems,

$$-C_D \frac{(\sigma^2)^{D/2}}{D} - \frac{T \operatorname{tr} I}{(4\pi)^{\frac{D-1}{2}} \Gamma\left(\frac{D-1}{2}\right)} \int_0^\infty \mathrm{d}q \, q^{D-2} \left[\ln\left(1 + e^{-\left(\sqrt{q^2+\sigma^2}+\mu\right)/T}\right) + (\mu \to -\mu)\right], \tag{2.56}$$

where $(\mu \to -\mu)$ represents the term where μ is replaced by $-\mu$ in the previous term. As can be seen from this expression, the contribution from a finite temperature does not include the divergence. The Matsubara sum has been performed and the integral over the momentum space remains. Thus, the effective potential at a finite temperature and a finite chemical potential reads

$$\begin{aligned} V(\sigma;T,\mu) =& \frac{1}{2}\left(\frac{1}{\lambda_r} + C_D(D-1)\right)\sigma^2\mu_r^{D-2} - C_D\frac{(\sigma^2)^{D/2}}{D} \\ & - \frac{T \operatorname{tr} I}{(4\pi)^{\frac{D-1}{2}} \Gamma\left(\frac{D-1}{2}\right)} \int_0^\infty \mathrm{d}q \, q^{D-2} \left[\ln\left(1 + e^{-\left(\sqrt{q^2+\sigma^2}+\mu\right)/T}\right) + (\mu \to -\mu)\right]. \end{aligned} \tag{2.57}$$

We have applied the same renormalization procedure (2.23) as in the model at zero temperature. This is because there is no divergence in the finite temperature term. The contribution from a finite temperature appears to push down the effective potential strongly near the origin and weakly away from the origin. As a result, the chiral symmetry gets restored continuously with increasing a temperature, and the second-order phase transition occurs.

To clarify the contribution from a finite chemical potential, we takes the zero temperature limit. At zero temperature, the expression is given by

$$V(\sigma; T \to 0, \mu) = \frac{1}{2}\left(\frac{1}{\lambda_r} + C_D(D-1)\right)\sigma^2\mu_r^{D-2} - C_D\frac{(\sigma^2)^{D/2}}{D} - \frac{\mathrm{tr}\, I}{(4\pi)^{\frac{D-1}{2}}\Gamma\left(\frac{D-1}{2}\right)}\int_0^\infty \mathrm{d}q\, q^{D-2}\left(|\mu| - \sqrt{q^2+\sigma^2}\right)\theta(|\mu| - \sqrt{q^2+\sigma^2}), \tag{2.58}$$

where $\theta(x)$ is a step function defined by $\theta(x) = 1$ for $x > 0$, and $\theta(x) = 0$ for $x < 0$. From this expression, the contribution from a chemical potential appears to push the effective potential down in a range, $|\sigma| < \mu$, without modifications of the shape of the effective potential outside the range, $|\sigma| > \mu$. The chiral symmetry can be restored discontinuously when a chemical potential becomes larger than a certain value (Shown in Fig. 2.10).

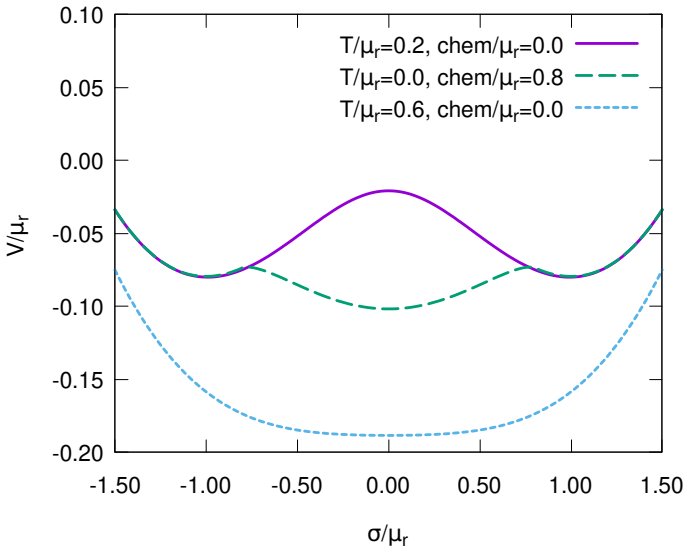

Fig. 2.10: Behavior of the effective potential at a finite temperature and chemical potential.

A phase diagram on a μ-T plane plotted by using Eq. (2.57) in two dimensions is shown in Fig. 2.11. In this calculation, the coupling is fixed so that the generated fermion mass normalized by μ_r is unity at zero temperature and chemical potential. A second-order phase transition boundary is drawn in high temperature and low chemical potential area, and the line ends at lower temperature and higher chemical potential; this point is called the critical end-

point. When the model becomes massive, the critical line disappears and a crossover region takes place. A first-order phase transition boundary exists in the massless and massive theory. The critical temperature where the chiral condensate vanishes at zero chemical potential is $e^{\gamma}/\pi \simeq 0.57$ (on the vertical axis) and the chemical potential where the condensate jump from a finite value to zero at zero temperature is $1/\sqrt{2} \simeq 0.71$ (on the horizontal axis) [107, 108]. Similarly in three dimensions, the former value is $1/\ln 4 \simeq 0.72$ and the latter is 1 [33, 109].

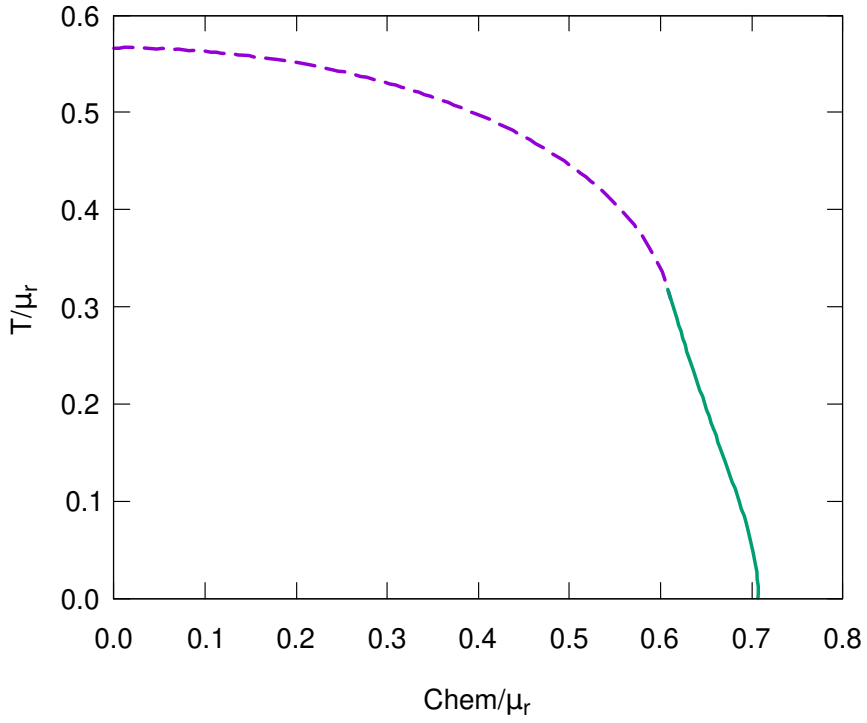

Fig. 2.11: Phase diagram on the μ-T plane in two dimensions. The solid and dashed lines show the first-order and second-order phase transition boundaries respectively. The chiral symmetry is broken inside the boundary and the chiral condensate vanishes outside.

Chapter 3

Finite-size Effect

We show finite-size effects on the dynamical chiral symmetry breaking by using a four-fermion interaction model. In this chapter, we consider a situation at zero temperature in the GN model based on our paper [81] (The GN model is also used in the next chapter.). The background spacetime where we analyze the finite-size effects is a $(D-1)$-dimensional Minkowski spacetime with a one-dimensional sphere, $\mathcal{M}^{D-1} \times \mathbb{S}^1$. To treat a theory with a finite-size space, one usually needs to consider a boundary condition. We impose a U(1)-valued boundary condition to fermions in the compactified direction,

$$\psi(x^0, x^1, \ldots, x^{D-1} + L) = e^{-i\pi\delta}\psi(x^0, x^1, \ldots, x^{D-1}), \tag{3.1}$$

with L denoting the size of $\mathbb{S}^1$ and δ a U(1) phase. In other words, going around the one-dimensional sphere, the fermion gets the U(1) phase, δ: $\delta = 0$ and 1 corresponding to periodic and anti-periodic boundary conditions, respectively. The phase, δ, is a parameter that is determined by conditions outside of the system or a non-trivial topology of the early universe. When we use the term finite-size effect, we include both contributions from a finite volume and a boundary condition.

3.1 Effective Potential Analysis

To analyze the theory with the compactified space, we follow the manner already described in Chapter 2.4 as treating a model at a finite temperature. This is because the imaginary time direction at finite temperature is also compactified to $\mathbb{S}^1$. The difference between the two lies in the boundary condition. To apply the following replacement in the effective potential at finite temperature (2.54),

$$\begin{cases} T & \to \dfrac{1}{L} \\ \tilde{\omega}_{\mu,n} & \to k_{\delta,n} = \dfrac{2\pi}{L}\left(n + \dfrac{\delta}{2}\right) \end{cases}, \tag{3.2}$$

we obtain the effective potential with the compactified space in the leading order of the $1/N$ expansion,

$$\begin{aligned} V(\sigma;L,\delta) =& \frac{1}{2}\left(\frac{1}{\lambda_r}+C_D(D-1)\right)\sigma^2\mu_r^{D-2}-C_D\frac{(\sigma^2)^{D/2}}{D} \\ & -\frac{2\,\mathrm{tr}\,I}{(4\pi)^{\frac{D-1}{2}}\Gamma\left(\frac{D-1}{2}\right)L}\int_0^\infty \mathrm{d}q\, q^{D-2}\mathrm{Re}\left[\ln\left(1+e^{-L\sqrt{q^2+\sigma^2}+i\pi\delta}\right)\right]. \end{aligned} \tag{3.3}$$

In the large size limit, $L\to\infty$, this effective potential returns to Eq. (2.28) and reproduces the theory without the compactified space. Because of the periodicity of the effective potential, $V(\sigma)|_\delta = V(\sigma)|_{\delta+2n\pi}$ $(n\in\mathbb{Z})$, it is enough to discuss the effective potential within the interval, $0\le\delta\le 1$ or $0\le\delta\le 2$.

In this massless model, it is convenient to use the solution of the gap equation at $L\to\infty$ instead of the renormalization scale, μ_r, to clarify finite-size effects. The expression of the effective potential rewritten by using the generated fermion mass (2.30) reads

$$\begin{aligned} \frac{V(\sigma;L,\delta)}{m_\alpha^D} =& C_D\left[\frac{(-1)^\alpha}{2}\left(\frac{\sigma}{m_\alpha}\right)^2-\frac{1}{D}\left(\frac{\sigma^2}{m_\alpha^2}\right)^{D/2}\right] \\ & -\frac{2\,\mathrm{tr}\,I}{(4\pi)^{\frac{D-1}{2}}\Gamma\left(\frac{D-1}{2}\right)Lm_\alpha}\int_0^\infty\frac{\mathrm{d}q}{m_\alpha}\left(\frac{q}{m_\alpha}\right)^{D-2}\mathrm{Re}\left[\ln\left(1+e^{-L\sqrt{q^2+\sigma^2}+i\pi\delta}\right)\right], \end{aligned} \tag{3.4}$$

where α is a parameter taking 0 or 1. m_0 is the usual dynamical mass in the large size limit, $L\to\infty$, for the strong coupling, $\lambda_r>\lambda_{c,D}$, (shown in Fig. 2.4), and m_1 is a mass parameter defined by an absolute value of the solution of the gap equation (2.30) for the weak coupling, $\lambda_r<\lambda_{c,D}$; as a result, the coupling constant is removed form this expression. Because the critical coupling is vanishing in two dimensions, $\lambda_{c,D=2}=0$, we can describe the dynamical chiral symmetry breaking for $D=2$ only by using m_0. Using this notation makes clear finite-size effects; in other words, if we observe chiral symmetry restoration (breaking) by using the effective potential written in m_0 (m_1), we find that it is due to the finite-size effects. The same applies to the situations at a finite temperature and a finite chemical potential (using the next chapter).

In the large size limit, $L\to\infty$ (Chapter 2), we have normalized the effective potential at the origin to $V(\sigma=0)=0$. This is the usual way to remove the zero-point energy that is divergent. However, when dealing with theories with a finite compactified space (as well as at a finite temperature), it is necessary to pay attention to how to remove the zero-point energy; this is the improvement from [50]. By using some formulae [90, 91, 109, 110], the effective potential with the finite size (3.4) at the origin, $\sigma=0$, is reduced to

$$V(\sigma=0;L,\delta)=\frac{\mathrm{tr}\,I}{(4\pi)^{\frac{D-1}{2}}}\frac{\Gamma(D)}{\Gamma\left(\frac{D+1}{2}\right)}\frac{\mathrm{Re}\left[\mathrm{Li}_D\left(e^{i\pi\delta}\right)\right]}{L^D}, \tag{3.5}$$

where $\mathrm{Li}_a(x)$ is the polylogarithm function defined by $\mathrm{Li}_s(z)=\sum_{n=1}^\infty n^{-s}z^n$. Thus, in the normalization we have adopted, the value of the effective potential at the origin depends on

the size, L, and the boundary condition, δ. In the large size limit, $L \to \infty$, or when the phase, δ, takes a certain value, the value of the effective potential at the origin becomes zero. Such a parameter dependence has a decisive contribution to the thermodynamic properties discussed later.

The behavior of the effective potential is plotted in Fig. 3.1 for a fixed size, $Lm_\alpha = 1.7$. Since the effective potential is axisymmetric, we show the region, $\sigma \geq 0$. We can observe that the effective potential lifts up and the position of the minimum moves away from the origin with varying the boundary condition form $\delta = 1$ (anti-periodic) to $\delta = 0$ (periodic) for both the strong coupling and the weak coupling. When the value of the effective potential at the origin is close to zero, this means that the finite-size effects is small. Therefore, the chiral symmetry tends to be restored near the anti-periodic boundary condition, $\delta = 1$, and enhanced near the periodic one, $\delta = 0$, for the fixed size, $Lm_\alpha = 1.7$. These results are consistent with Ref. [34, 42, 43, 111].

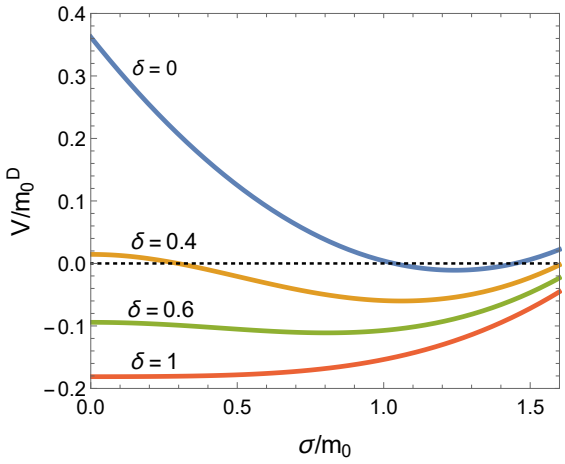

(a) $D = 2$, $\lambda_r > \lambda_{c,D}(\alpha = 0)$

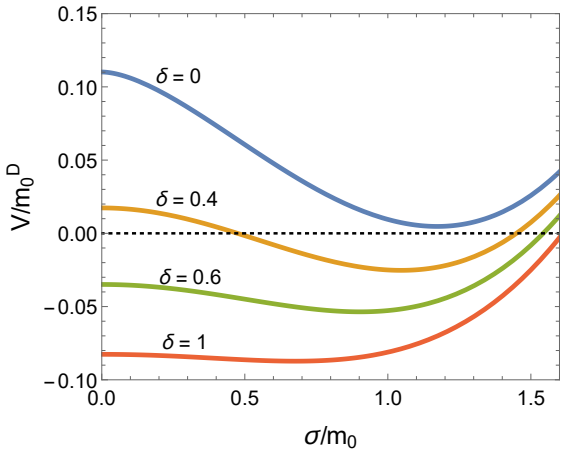

(b) $D = 3$, $\lambda_r > \lambda_{c,D}(\alpha = 0)$

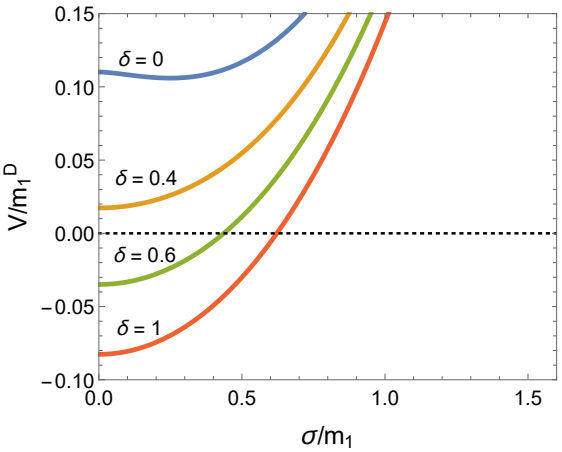

(c) $D = 3$, $\lambda_r < \lambda_{c,D}(\alpha = 1)$

Fig. 3.1: The effective potential as a function of σ for $Lm_\alpha = 1.7$. The two figures on the left are in the strong coupling, $\lambda_r > \lambda_{c,D}$ $(\alpha = 0)$, and the figure on the right is in the weak coupling, $\lambda_r < \lambda_{c,D}$ $(\alpha = 1)$.

3.2 Generated Fermion Mass

The dynamically generated fermion mass, denoted by m, is given by the minimum of the effective potential, $V(\sigma; L, \delta)$. As reviewed in Chapter 2.2, this is obtained as a non-trivial solution of the gap equation,

$$\left.\frac{\partial V(\sigma; L, \delta)}{\partial \sigma}\right|_{\sigma=m} = 0. \tag{3.6}$$

Since an exact solution can not be obtained, we evaluate the gap equation (3.6) numerically and plot the behavior of the generated fermion mass as a function of the phase, δ, and the size, L. In Fig. 3.2, the behavior of the generated fermion mass as a function of δ for the fixed size, $Lm_\alpha = 1.7$. For the strong coupling, $\lambda_r > \lambda_{c,D}$, it is seen that the generated

fermion mass monotonically decreases as the phase approaches one, $\delta \to 1$; in particular, the chiral symmetry gets restored as the second-order phase transition in two dimensions. Near the periodic boundary condition, the chiral symmetry breaking is enhanced ($m/m_0 > 1$), and even for the weak coupling, $\lambda_r < \lambda_{c,D}$, observed in the narrow regions.

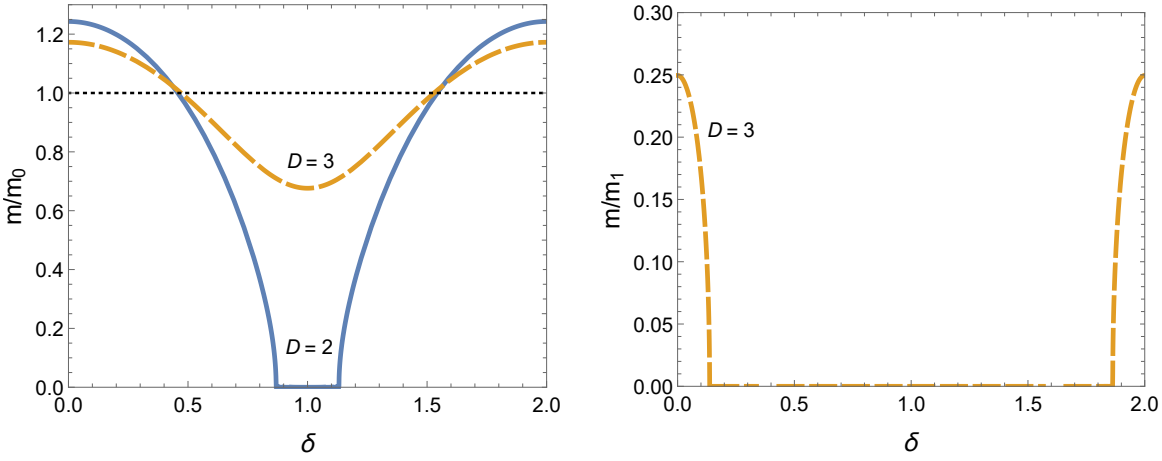

(a) $\lambda_r > \lambda_{c,D}(\alpha = 0)$, $Lm_0 = 1.7$ (b) $\lambda_r < \lambda_{c,D}(\alpha = 1)$, $Lm_1 = 1.7$

Fig. 3.2: The dynamically generate fermion mass as a function of δ (left: strong coupling, and right: weak coupling). The blue solid curves is in two dimensions, and the orange dashed curve in three dimensions.

In Fig. 3.3, the behavior of the generated fermion mass is shown as a function of L. At the periodic boundary condition, $\delta = 0$, the dynamical mass increases with decreasing the size, L, and the chiral symmetry breaking is enhanced; as a result, the dynamical mass diverges in the small size limit, $L \to 0$. In contrast, at the anti-periodic boundary condition, $\delta = 1$, the finite-size effect restores the broken chiral symmetry as the second-order phase transition. At $\delta = 0.4$ for the strong coupling, the behavior of the generated mass indicates features of both the periodic and anti-periodic boundary conditions. In this case, the generated fermion mass converges to 1 from above in the large size limit, $m/m_0 \to 1^+$ for $L \to \infty$, but the chiral symmetry is restored in the small size limit, $m/m_0 \to 0$ for $L \to 0$.

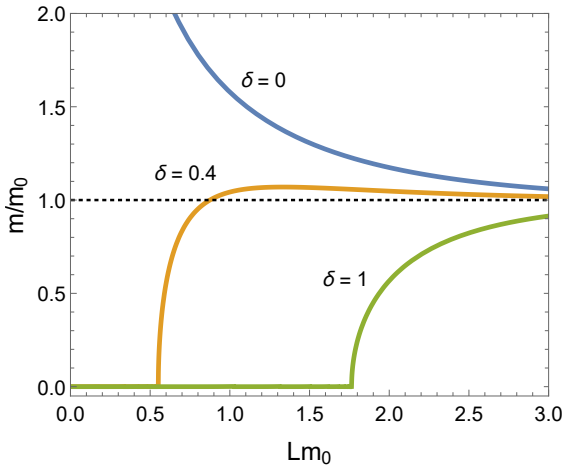

(a) $D = 2$, $\lambda_r > \lambda_{c,D}(\alpha = 0)$

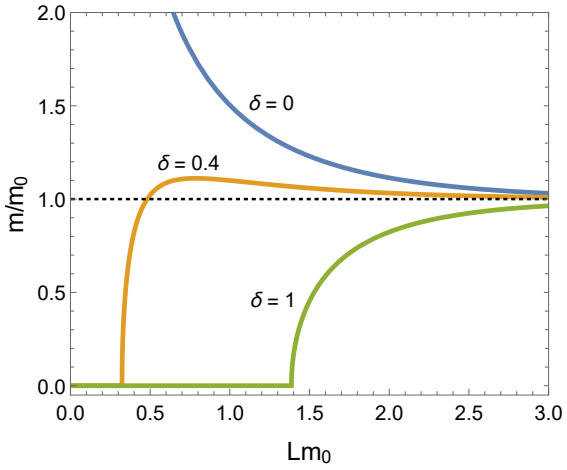

(b) $D = 3$, $\lambda_r > \lambda_{c,D}(\alpha = 0)$

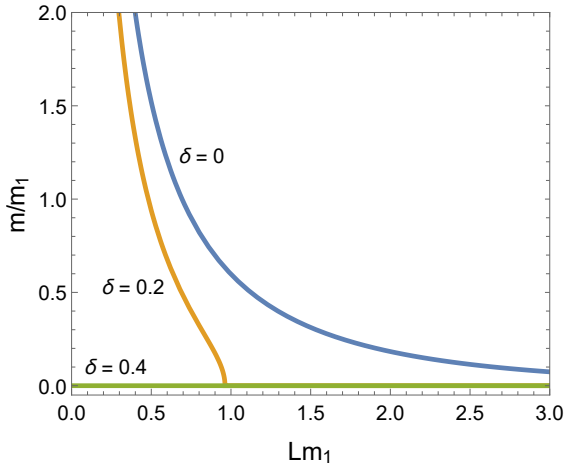

(c) $D = 3$, $\lambda_r < \lambda_{c,D}(\alpha = 1)$

Fig. 3.3: The dynamically generated fermion mass as a function of L. The two figures on the left are in the strong coupling, $\lambda_r > \lambda_{c,D}$ $(\alpha = 0)$, and the figure on the right is in the weak coupling, $\lambda_r < \lambda_{c,D}$ $(\alpha = 1)$.

Since the order of the phase transition is second order, the phase boundary is obtained in the chiral limit, $m \to 0$, of the gap equation, in the same way as Eq. (2.26). The critical length, denoted by $L_{\rm cr}$, that divides the symmetric and broken phases is given by

$$L_{\rm cr} m_\alpha = \begin{cases} 2\pi \left[\dfrac{2(-1)^\alpha}{\sqrt{\pi}} \dfrac{\Gamma\left(\frac{3-D}{2}\right)}{\Gamma\left(1-\frac{D}{2}\right)} \zeta\left(3-D\right) \right]^{\frac{1}{D-2}} & (\delta = 0, 2) \\ 2\pi \left[\dfrac{(-1)^\alpha}{\sqrt{\pi}} \dfrac{\Gamma\left(\frac{3-D}{2}\right)}{\Gamma\left(1-\frac{D}{2}\right)} \left(\zeta\left(3-D, \dfrac{\delta}{2}\right) + \zeta\left(3-D, 1-\dfrac{\delta}{2}\right) \right) \right]^{\frac{1}{D-2}} & (0 < \delta < 2) \end{cases}, \tag{3.7}$$

where $\zeta(s)$ is the Riemann zeta function, and $\zeta(s, a)$ is the Hurwitz zeta function defined by $\zeta(s, a) = \sum_{n=0}^{\infty} (n + a)^{-s}$: $\zeta(s, 1) = \zeta(s)$. At the anti-periodic boundary condition, $\delta = 1$,

this formula coincides with the one of the critical temperature that is derived in Ref. [109]: $L_{\rm cr}m_0 \simeq 1.76$ for $(D,\delta) = (2,1)$, and $L_{\rm cr}m_0 = \ln 4 \simeq 1.39$ for $(D,\delta) = (3,1)$.

By using the critical length (3.7), the phase diagram is plotted on a δ-L plane in Fig. 3.4. For the strong coupling, $\lambda_r > \lambda_{c,D}$, the chiral symmetric phase can be observed around the anti-periodic boundary condition, $\delta = 1$, while only the broken phase is observed at the periodic boundary condition, $\delta = 0$. For the weak coupling, $\lambda_r < \lambda_{c,D}$, the chiral symmetry is broken near the periodic boundary condition, and the critical length is divergent at $\delta = 0$ and 2 in three dimensions. As long as the size is finite, $L < \infty$, the chiral symmetry is always broken at the periodic boundary condition. It can be also observed that the finite-size effect is more suppressed, and the critical length is smaller in three dimensions than two dimensions.

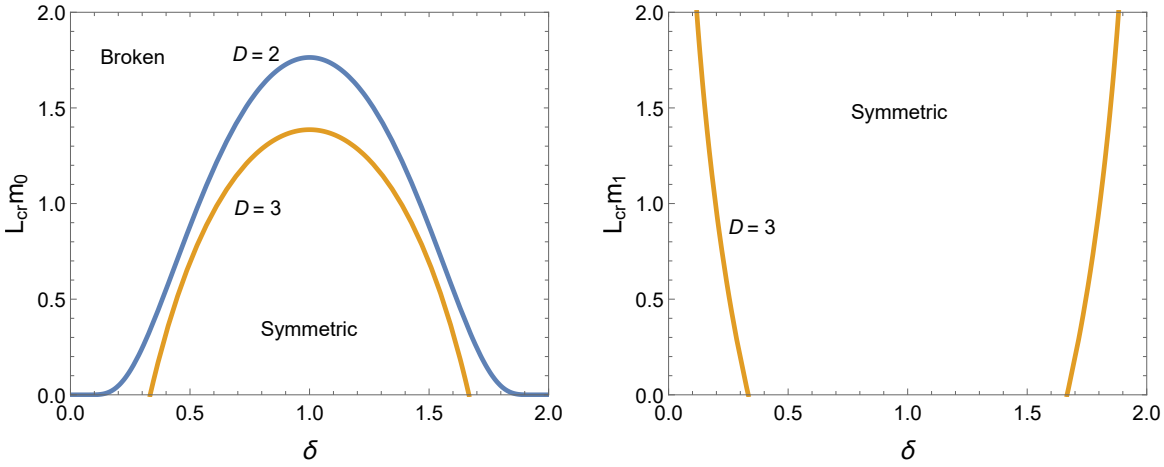

(a) $\lambda_r > \lambda_{c,D}(\alpha = 0)$ (b) $\lambda_r < \lambda_{c,D}(\alpha = 1)$

Fig. 3.4: The phase diagram on a δ-L (left: strong coupling, and right: weak coupling). The chiral symmetry is restored below the curves for $\lambda_r > \lambda_{c,D}$, and between the curves for $\lambda_r < \lambda_{c,D}$.

3.3 Casimir Effect

To consider a finite-size effect in the four-fermion interaction model on $\mathcal{M}^{D-1}\times\mathbb{S}^1$, we evaluate a response for the size given by the first derivative of the effective potential with respect to L,

$$T(L,\delta) = -\left.\frac{\partial V(\sigma;L,\delta)}{\partial L}\right|_{\sigma=m}, \tag{3.8}$$

where m is the fermion mass that is given by the minimum of the effective potential, $V(\sigma;L,\delta)$. $T(L,\delta)$ is a string tension. Because the effective potential is a thermodynamic potential density, the string tension is also a thermodynamic quantity. By using this thermodynamic quantity, we discuss the phase transition and the stability of the system.

The explicit expression of the string tension reads

$$\frac{T(L,\delta)}{m_\alpha^{D+1}} = -\frac{2\,\mathrm{tr}\,I}{(4\pi)^{\frac{D-1}{2}}\Gamma\left(\frac{D-1}{2}\right)(Lm_\alpha)^2}\int_0^\infty \frac{\mathrm{d}q}{m_\alpha}\left(\frac{q}{m_\alpha}\right)^{D-2} \times \mathrm{Re}\left[\ln\left(1+e^{-L\sqrt{q^2+m^2}+i\pi\delta}\right)+\frac{L\sqrt{q^2+m^2}}{1+e^{L\sqrt{q^2+m^2}-i\pi\delta}}\right]. \tag{3.9}$$

In Fig. 3.5, the behavior of the string tension is shown as a function of the phase, δ, for a fixed length, $Lm_\alpha = 1.7$. For the strong coupling, $\lambda_r > \lambda_{c,D}$, sharp bends appear on the blue curve (in two dimensions) near $\delta = 1$. These sharp bends are observed at the same boundary conditions where the chiral phase transition occurs in Fig. 3.2. On the other hand, it is shown that the string tension is repulsive at the periodic boundary condition, $\delta = 0$ and 2, and the tension monotonically decreases as approaching the anti-periodic boundary condition, $\delta = 1$. During this decreasing, the sign of the tension, $T(L,\delta)$, changes near $\delta \sim 0.5$. An attractive string tension is realized near the periodic boundary condition.

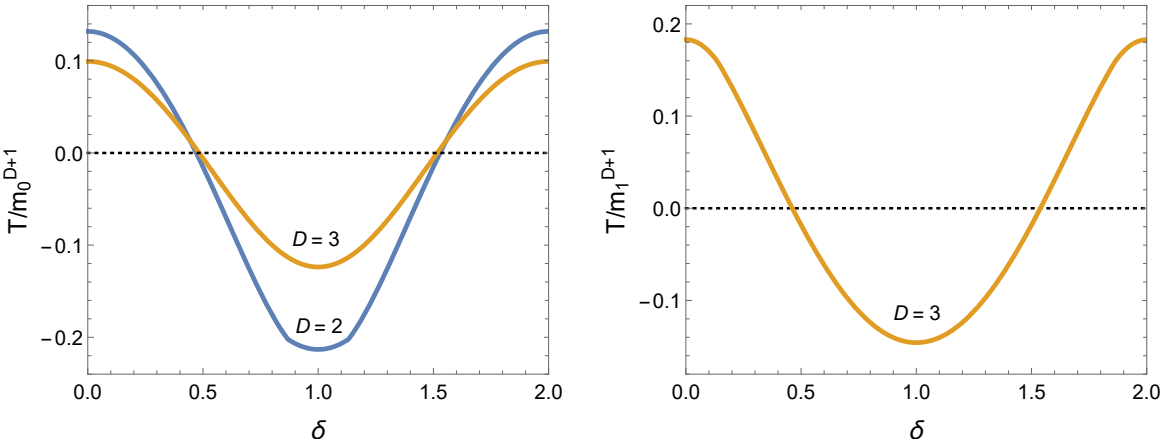

(a) $\lambda_r > \lambda_{c,D}(\alpha = 0)$, $Lm_0 = 1.7$ (b) $\lambda_r < \lambda_{c,D}(\alpha = 1)$, $Lm_1 = 1.7$

Fig. 3.5: The string tension as a function of δ for a fixed length $Lm_\alpha = 1.7$ (left: strong coupling, and right: weak coupling).

Next, we plot the behavior of the string tension as a function of the size, L, in Fig. 3.6. This string tension diverges and vanishes in the small and large size limit, $L \to 0$ and $L \to \infty$, respectively. At the periodic (anti-periodic) boundary condition, $\delta = 0$ ($\delta = 1$), the tension remains repulsive (attractive) and monotonically decreases (increases) with increasing the size, L. A sharp bend appears on the orange curve ($\delta = 0.4$) in Fig. 3.6 (a). From comparison with Fig. 3.3, this bend exhibits the phase transition. The sign flip seen in Fig. 3.5 is not observed in Fig. 3.6.

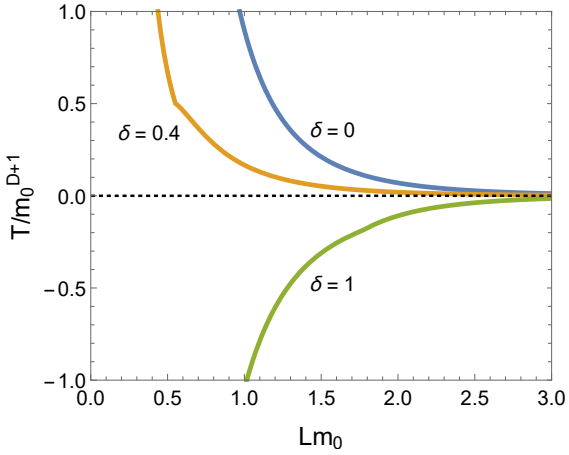

(a) $D = 2$, $\lambda_r > \lambda_{c,D}(\alpha = 0)$

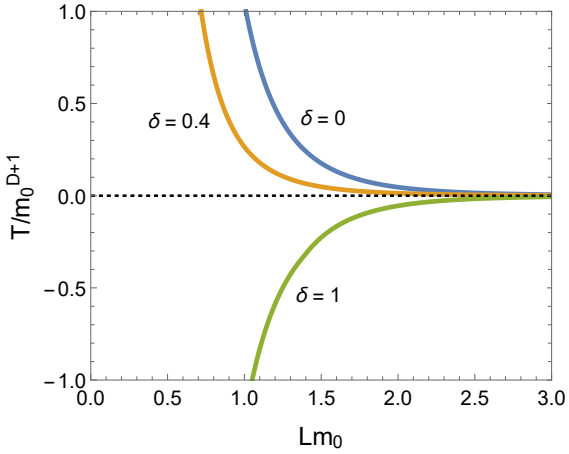

(b) $D = 3$, $\lambda_r > \lambda_{c,D}(\alpha = 0)$

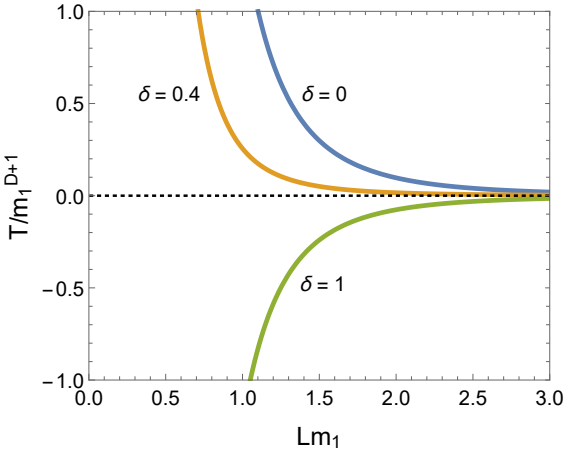

(c) $D = 3$, $\lambda_r < \lambda_{c,D}(\alpha = 1)$

Fig. 3.6: The string tension as a function of L. The two figures on the left are in the strong coupling, $\lambda_r > \lambda_{c,D}$ $(\alpha = 0)$, and the figure on the right is in the weak coupling, $\lambda_r < \lambda_{c,D}$ $(\alpha = 1)$.

In order to clarify the sign-flip points of the string tension, we numerically solve $T(L, \delta) = 0$. The results of this numerical calculation are plotted in Fig. 3.7. Since the sign-flip boundaries appear in limited ranges of the phase, $0.4 < \delta < 0.5$ and $1.5 < \delta < 1.6$, we show only the range, $0.4 < \delta < 0.5$. The string tension is repulsive and attractive on the left and right side of the curve, respectively. For the strong coupling, $\lambda_r > \lambda_{c,D}$, the sign-flip boundary asymptotically approaches $\delta = 0.5$ as the size increases. Referring the phase diagram (Fig. 3.4), the system with the compactified space larger than $Lm_0 \simeq 0.5$ is in the broken phase, and this behavior of the sign-flip boundary is caused by the generated fermion mass; in other words, the generated fermion mass extends the domain where the repulsive tension is induced. For $Lm_0 \lesssim 0.5$, the system is in the chiral symmetric phase, and then the boundary is represented by a vertical line. In the symmetric phase, the expression of the string tension (3.9) can be

D	2	3
δ	0.423	0.462

Tab. 3.1: The phase δ where the sign of the string tension flips in the symmetric phase.

reduced to

$$\frac{T(L,\delta)_{\rm sym}}{m_\alpha^{D+1}} = \frac{\mathrm{tr}\, I}{(4\pi)^{D-1}} \frac{\Gamma\left(D+1\right)}{\Gamma\left(\frac{D+1}{2}\right)} \frac{\mathrm{Re}\left[\mathrm{Li}_D\left(e^{i\pi\delta}\right)\right]}{(Lm_\alpha)^{D+1}}. \tag{3.10}$$

From this expression, it is clear that the solution of $T(L,\delta)_{\rm sym} = 0$ is independent of L as long as L is finite, and given by

$$\mathrm{Re}\left[\mathrm{Li}_D\left(e^{i\pi\delta}\right)\right] = 0. \tag{3.11}$$

The specific value of the sigh-flip phase is shown in Tab. 3.1.

For the weak coupling, $\lambda_r < \lambda_{c,D}$, the sign-flip boundary for arbitrary $Lm_1(< \infty)$ is determined by the equation (3.11) because, as can be seen from Fig. 3.4, the system is in the chiral symmetric phase.

Through the discussions of the string tension, it is found that the string tension is only repulsive (attractive) near the periodic (anti-periodic) boundary condition. Therefore, near both the boundary conditions, the compactified space can not remains finite. While the sign-flip point exists at the intermediate boundary condition, $0.4 < \delta < 0.5$, as we have shown, this point does not means a stable size. The stable size we call is the point where the string tension becomes negative with increasing the system size and positive with decreasing the system size. This is because when the size of the compactified space becomes larger (smaller) than this point, the tension becomes repulsive (attractive). Here, let us go back to the discussion in Chapter. 3.1. At the periodic (anti-periodic) boundary condition, the effective potential at a finite size is larger than the one in the large (small) limit, $L \to \infty$ ($L \to 0$), which is consistent with the string tension being repulsive (attractive).

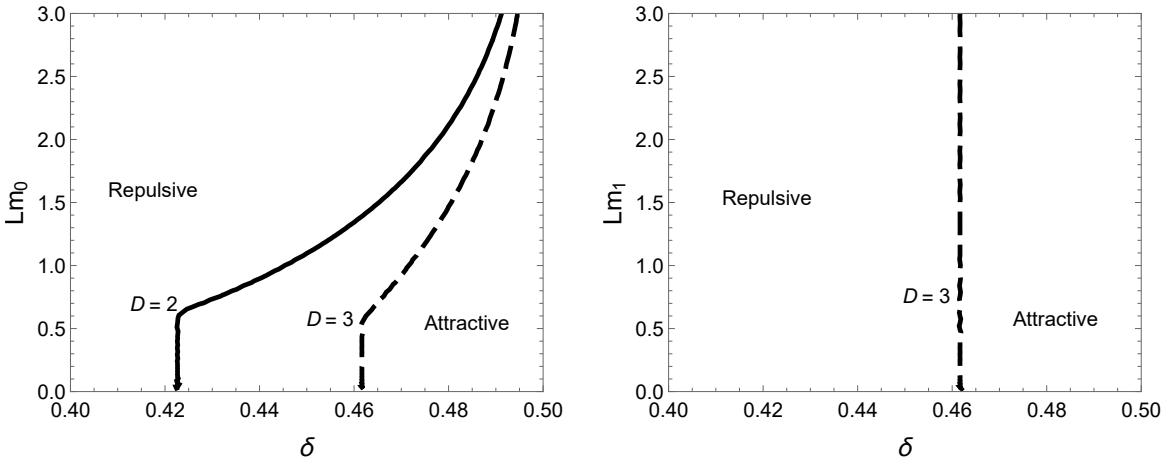

(a) $\lambda_r > \lambda_{c,D}(\alpha = 0)$, $Lm_0 = 1.7$ (b) $\lambda_r < \lambda_{c,D}(\alpha = 1)$, $Lm_1 = 1.7$

Fig. 3.7: The sign-flip boundaries between the repulsive (left side of the curves) and attractive (right side of the curves) tension on a δ-L plane.

We have discussed dynamical chiral symmetry breaking in the GN model on $\mathcal{M}^{D-1} \times \mathbb{S}^1$ with the U(1)-valued boundary condition. Assuming the homogeneous chiral condensate and using the zeta function regularization, we have obtained the explicit expression of the effective potential for the vacuum expectation value of the fermion and anti-fermion composite field in the leading order of the $1/N$ expansion.

In particular, we have focused on the topological effect stemming from the boundary condition at zero temperature. We calculated the dynamically generated fermion mass as a function of L and δ, and checked that only the second-order phase transition occurs. The phase diagram has shown on a δ-L plane for the strong and weak couplings in Fig. 3.4.

To find a phenomenological consequence, we has discussed a string tension as the Casimir effect in the model on $\mathcal{M}^{D-1} \times \mathbb{S}^1$. The critical lengths for chiral symmetry breaking are observed as slightly sharp bends of the string tension. Moreover, we have found the explicit expression for the sign-flip points in the symmetric phase, and the boundary lines dividing the repulsive tension and attractive tension on the L-δ plane, Fig. 3.7. The phase transition is observed as sharp bends in Fig. 3.7 (a). However, following our analysis, there is no stable size for the string tension in the four-fermion interaction model at zero temperature.

Chapter 4

Thermal and Finite-size Effects

In the preceding chapter, we have discussed finite-size effects in the GN model at zero temperature. We here consider finite-size effects in the GN model at a finite temperature and a finite chemical potential.

4.1 Effective Potential Analysis

Let us derive the effective potential in the leading order of the $1/N$ expansion on a D-dimensional background spacetime, $\mathbb{R}^{D-2} \times \mathbb{T}^2$, a torus $\mathbb{T}^2 \simeq \mathbb{S}^1 \times \mathbb{S}^1$, with a finite-size space at a finite temperature. The formulation at a finite temperature and a finite chemical potential is based on the discussion in Chapter 2.4.

The action of the model is

$$S_{\mathrm{GN},L,T} = \int \mathrm{d}^{D-2}x \int_0^L \mathrm{d}x^{D-1} \int_0^{1/T} \mathrm{d}x^D \left[\bar{\psi}(x)\tilde{\gamma}^k(\partial_k + \mu\delta_k^D)\psi(x) - \frac{\lambda_0}{2N}(\bar{\psi}(x)\psi(x))^2\right], \tag{4.1}$$

with the U(1)-valued boundary condition in the compactified direction,

$$\psi(x^1, \ldots, x^{D-1} + L, x^D) = e^{-i\pi\delta}\psi(x^1, \ldots, x^{D-1}, x^D), \tag{4.2}$$

the anti-periodic boundary condition in the imaginary time direction,

$$\psi(x^1, \ldots, x^{D-1}, x^D + 1/T) = -\psi(x^1, \ldots, x^{D-1}, x^D), \tag{4.3}$$

and a chemical potential, μ. Applying the same procedures described in Chapter 2.1 and 2.2, we obtain the effective potential in the leading order of the $1/N$ expansion,

$$V(\sigma; L, \delta, T, \mu) = \frac{\sigma^2}{2\lambda_0} - \frac{\mathrm{tr}\, I}{2}\frac{T}{L}\sum_{n,n'=-\infty}^{\infty}\int \frac{\mathrm{d}^{D-2}\boldsymbol{k}}{(2\pi)^{D-2}} \ln\left(\boldsymbol{k}^2 + k_{\delta,n}^2 + \tilde{\omega}_{\mu,n'}^2 + \sigma^2\right). \tag{4.4}$$

There are two sums: quantized momenta, $k_{\delta,n}$, on the compactified direction and the Matsubara frequencies, $\tilde{\omega}_{\mu,n'}$, on the imaginary-time direction.

By using the identity related to the zeta function regularization (2.17) again, the second term in this expression (4.4) is separated into a non-thermal part and a thermal part by performing the Matsubara sum. We takes the sum over the momentum space in the non-thermal term, while the sum in the thermal term are left. The expression of the effective potential on $\mathbb{R}^{D-2} \times \mathbb{T}^2$ reads

$$\begin{aligned}
&V(\sigma; L, \delta, T, \mu) \\
=&\frac{1}{2}\left(\frac{1}{\lambda_r} + C_D(D-1)\right)\sigma^2\mu_r^{D-2} - C_D\frac{(\sigma^2)^{D/2}}{D} \\
&- \frac{2\,\mathrm{tr}\,I}{\tilde{C}_{D+1}L}\int_0^\infty \mathrm{d}q\, q^{D-2}\mathrm{Re}\left[\ln\left(1 + e^{-L\sqrt{q^2+\sigma^2}+i\pi\delta}\right)\right] \\
&- \frac{\mathrm{tr}\,I}{\tilde{C}_D}\frac{T}{L}\sum_{n=-\infty}^{\infty}\int_0^\infty \mathrm{d}q\, q^{D-3}\left[\ln\left(1 + e^{-\left(\sqrt{q^2+k_{\delta,n}^2+\sigma^2}+\mu\right)/T}\right) + (\mu \to -\mu)\right],
\end{aligned} \tag{4.5}$$

with a constant, $\tilde{C}_D = (4\pi)^{D/2-1}\Gamma\left(D/2-1\right)$. In this expression, the coupling of the four-fermion interaction is also renormalized by the same procedure (2.23) since these extensions with L, δ, T, and μ have nothing to do with the UV divergence. The second term represents the contribution from the vacuum, the third term the pure contribution from finite size, and the last term the contribution from finite size, a finite temperature, and a finite chemical potential. The first through third terms are the same as the effective potential with the compactified space (3.3). We can confirm that this effective potential (4.5) reproduces the one at a finite temperature and a finite chemical potential (2.57) in the large size limit, $L \to \infty$, and the one with the compactified space (3.3) at zero temperature and zero chemical potential, $T = \mu = 0$.

We are interested in the situation in which the chiral symmetry is broken in the large size limit, $L \to \infty$. As is mentioned in Chapter 3.1, the normalized coupling, λ_r, and the normalization scale, μ_r, can be removed from Eq. (4.5) by using the generated fermion mass, m_0, on $\mathcal{M}^D$. The expression (4.5) is simplified to

$$\begin{aligned}
&\frac{V(\sigma; L, \delta, T, \mu)}{m_0^D} \\
=&C_D\left[\frac{1}{2}\left(\frac{\sigma}{m_0}\right)^2 - \frac{1}{D}\left(\frac{\sigma^2}{m_0^2}\right)^{D/2}\right] \\
&- \frac{2\,\mathrm{tr}\,I}{\tilde{C}_{D+1}Lm_0}\int_0^\infty \frac{\mathrm{d}q}{m_0}\left(\frac{q}{m_0}\right)^{D-2}\mathrm{Re}\left[\ln\left(1 + e^{-L\sqrt{q^2+\sigma^2}+i\pi\delta}\right)\right] \\
&- \frac{\mathrm{tr}\,I}{\tilde{C}_D}\frac{Tm_0^{-1}}{Lm_0}\sum_{n=-\infty}^{\infty}\int_0^\infty \frac{\mathrm{d}q}{m_0}\left(\frac{q}{m_0}\right)^{D-3}\left[\ln\left(1 + e^{-\left(\sqrt{q^2+k_{\delta,n}^2+\sigma^2}+\mu\right)/T}\right) + (\mu \to -\mu)\right].
\end{aligned} \tag{4.6}$$

In the following, we numerically evaluate this effective potential (4.6) in two and three dimensions in the framework of the dimensional regularization. In Fig. 4.1, the typical behavior of the effective potential is shown as a function of σ/m_0 for a fixed size, $Lm_0 = 1.5$, at the

periodic boundary condition, $\delta = 0$; only positive are is shown due to the axisymmetric. For $\mu/m_0 = 0$ (left in Fig. 4.1), the minimum is located at $\sigma/m_0 > 1$ by the finite-size effect at $\delta = 0$, and smoothly approaches the origin, $\sigma/m_0 = 0$, by the thermal effect with increasing T/m_0. For $\mu/m_0 = 0.7$ and 0.9 (right in Fig. 4.1), the other minimum appears at the origin for $T/m_0 = 0.1$ and 0.2. As mentioned in Chapter 3.1, we do not normalized the effective potential as $V(\sigma = 0; L, \delta, T, \mu) = 0$. Our normalization makes it easy to regard the minimum of the effective potential as a thermodynamic potential.

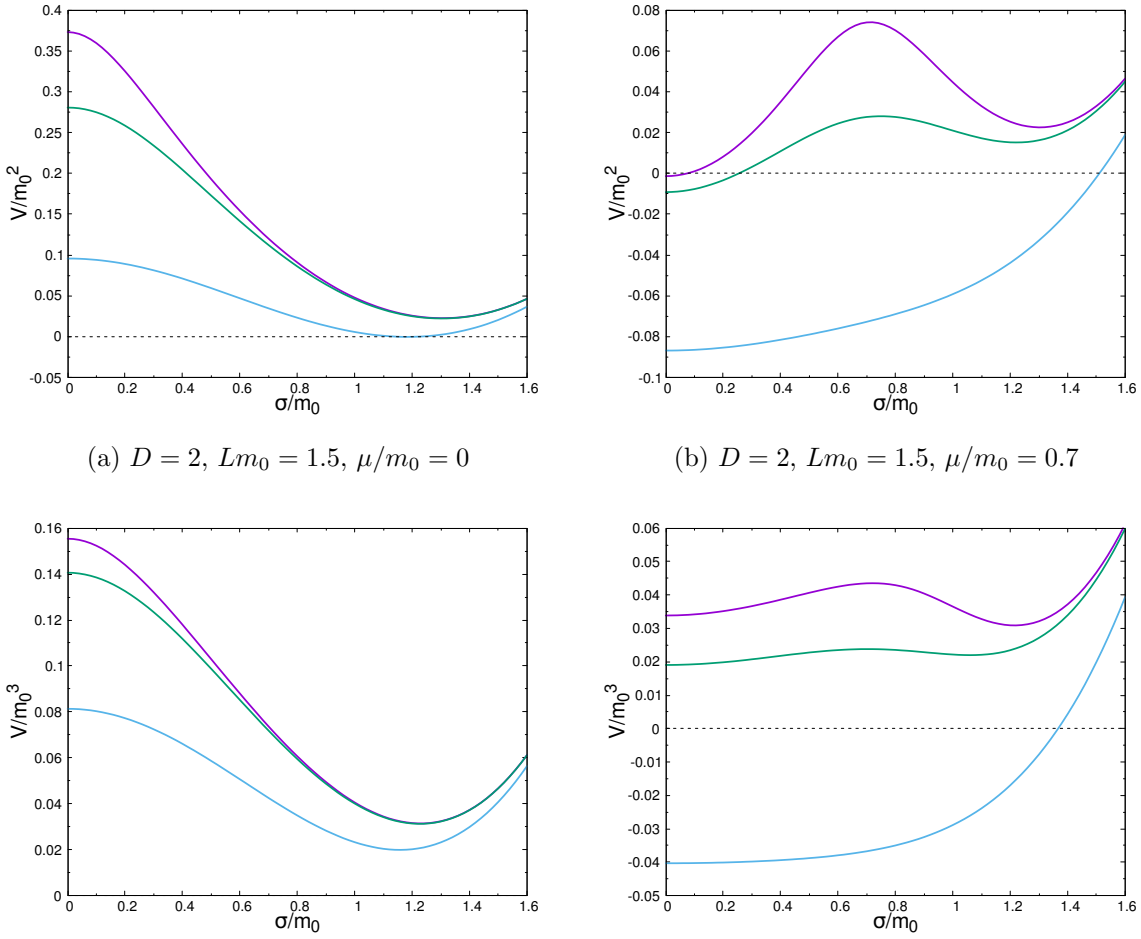

(a) $D = 2$, $Lm_0 = 1.5$, $\mu/m_0 = 0$

(b) $D = 2$, $Lm_0 = 1.5$, $\mu/m_0 = 0.7$

(c) $D = 3$, $Lm_0 = 1.5$, $\mu/m_0 = 0$

(d) $D = 3$, $Lm_0 = 1.5$, $\mu/m_0 = 0.9$

Fig. 4.1: The behavior of the effective potential for each chemical potential (above: $D = 2$, and below: $D = 3$) for $Lm_0 = 1.5$ and $\delta = 0$ (purple: $T/m_0 = 0.1$, green: $T/m_0 = 0.2$, and light blue: $T/m_0 = 0.4$).

4.2 Phase Structure

An order parameter of chiral symmetry breaking is given by the expectation value of the composite operator of the fermion and anti-fermion, $\langle\bar{\psi}\psi\rangle$. As long as we consider the mass-

less theory, the quantity is proportional to the auxiliary field, σ, in the ground state. One finds this state by evaluating the global minimum of the effective potential that satisfies $V(m; L, \delta, T, \mu) \leq V(\sigma; L, \delta, T, \mu)$ for any σ; the value of the minimum, m, is equivalent to a generated fermion mass. On the other hand, the local minima of the effective potential implies the existence of metastable states. The metastable states as well as the ground state has some phenomenological consequences. We assume a spatially homogeneous ground state as same as the previous sections and evaluate the number of extrema. In that sense, our results do not directly indicate the presence of the inhomogeneous phase, but the ground state can be inhomogeneous in the existence of multiple minima in a certain region of a parameter space.

Phase diagrams

In order to find a precise phase structure of the GN model, we evaluate not only the global minima but also the local minima of the effective potential, and hence we plot bifurcation diagrams. Since we consider the massless theory, the effective potential is an even function of σ. We classify the states by (i) the number of extrema and (ii) the position of the minimum of the effective potential for $\sigma \geq 0$. In this chapter, the class of the state is described by two symbols that we introduce: ${}^{\mathsf{a}}_{\mathsf{b}}\mathsf{S}$ and ${}^{\mathsf{a}}_{\mathsf{b}}\mathsf{B}$. The former and the latter denote a symmetric phase and a broken phase, respectively. The superscript a is the number of extrema for $\sigma \geq 0$ and the subscript b is the number of the extrema from the origin to the minimum, i.e. the bth extremum is the minimum and $\mathsf{b} \leq \mathsf{a}$. As an example, we show the phase diagram on the μ-T plane divided into four areas for $D = 3$, $Lm_0 = 8.0$ and $\delta = 1.0$. The correspondences between the symbol and behavior of the effective potential are indicated in Fig. 4.2. The symmetric phase ${}^{1}_{1}\mathsf{S}$ corresponding to (s) as the behavior of the effective potential, is realized at a high temperature and chemical potential, outside the outer boundary. On the outer boundary, only a second-order phase transition takes place. The broken phase, inside the outer boundary, contains three areas identified by the by the number of the extrema and the position of the minimum. A jump of the generated fermion mass between finite values is observed on the boundary between (b1), ${}^{4}_{4}\mathsf{B}$, and (b2), ${}^{4}_{2}\mathsf{B}$.

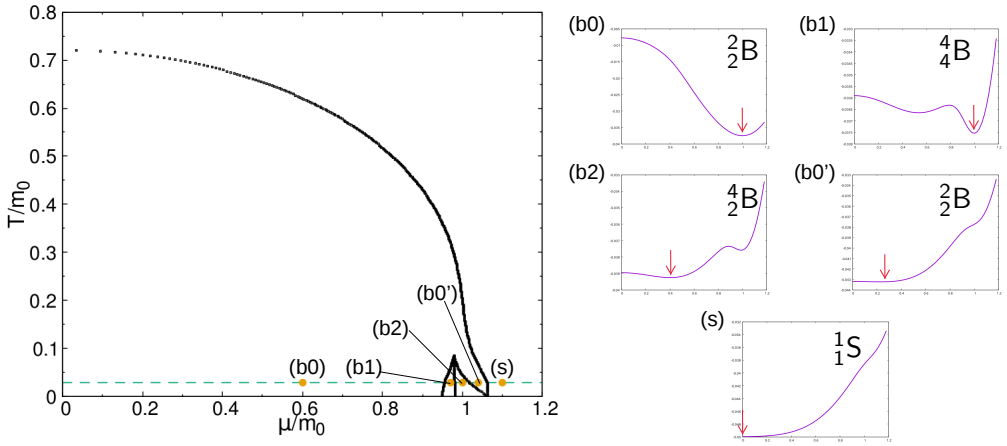

Fig. 4.2: Phase diagram on the μ-T plane ($D = 3.0$, $Lm_0 = 8.0$ and $\delta = 1.0$) and behavior of the effective potential along the dashed line ($T/m_0 = 0.03$). The arrows indicate the position of the minimum.

Although we can also treat intermediate value boundary conditions, we analyze the phase structure at the periodic ($\delta = 0$) and anti-periodic ($\delta = 1$) boundary conditions for simplicity. The phase diagrams on the μ-T plane for some fixed sizes and boundary conditions in Figs. 4.3 ($D = 2$) and 4.4 ($D = 3$); the bottom figures are plotted at a larger size than the top figures. As is mentioned in Chapter 2.4, it is known that, on usual non-compactified spaces $\mathbb{R}$ and $\mathbb{R}^2$, the critical temperatures at zero chemical potential are $e^\gamma/\pi \simeq 0.57$ ($D = 2$) and $1/\ln 4$ ($D = 3$), and the chemical potentials where the generated fermion mass jumps at zero temperature are $1/\sqrt{2} \simeq 0.71$ ($D = 2$) and 1 ($D = 3$) with the normalization by m_0. The finite-size effects primarily appear at a low temperature with a high chemical potential, and a high temperature with a low chemical potential. The effects of the boundary conditions are suppressed for a large size, but at a certain size prominently appear.

For instance, in two dimensions at $Lm_0 = 8.0$ and $\delta = 0.0$ (Fig. 4.3, bottom left), we can observe the complex behavior of the boundaries. As the chemical potential increases at a low temperature, the domain changes ${}^4_4\mathrm{B} \to {}^5_5\mathrm{B} \to {}^5_3\mathrm{B} \to {}^5_1\mathrm{S} \to {}^3_1\mathrm{S} \to {}^1_1\mathrm{S}$ and mass jumps appear twice on the boundaries ${}^5_5\mathrm{B} \to {}^5_3\mathrm{B}$ and ${}^5_3\mathrm{B} \to {}^5_1\mathrm{S}$.

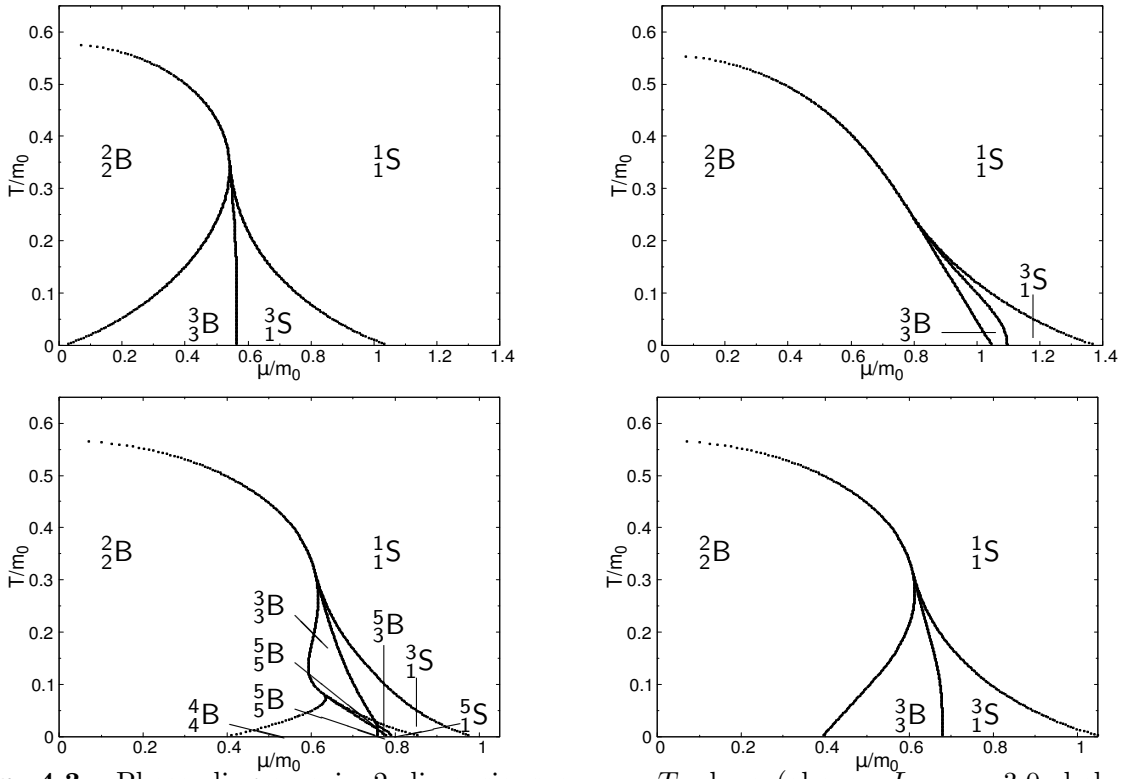

Fig. 4.3: Phase diagrams in 2 dimensions on a μ-T plane (above: $Lm_0 = 3.0$, below: $Lm_0 = 8.0$) for $\delta = 0.0$ (lefts) and $\delta = 1.0$ (rights).

The basic properties are common between two and three dimensions. Their differences come from the continuous momentum in the additional non-compactified space, $\mathbb{R}$. At $Lm_0 = 4.0$ and $\delta = 0.0$ in three dimensions (Fig. 4.4, bottom left), only the second-order phase transition takes place, and no critical end-point appears on the boundary dividing the symmetric and the broken phases. In the broken phase, the generated fermion mass discontinuously changes on the boundary between the areas, ${}^4_4\mathrm{B}$ and ${}^4_2\mathrm{B}$.

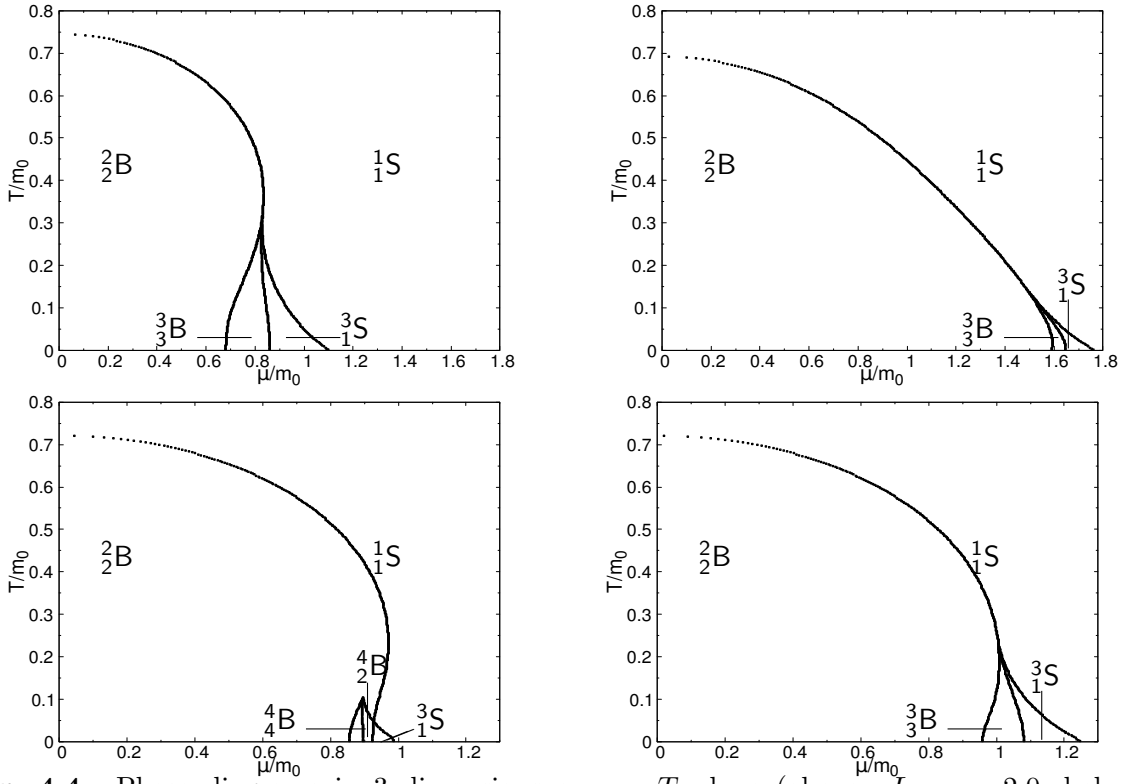

Fig. 4.4: Phase diagrams in 3 dimensions on a μ-T plane (above: $Lm_0 = 2.0$, below: $Lm_0 = 4.0$) for $\delta = 0.0$ (lefts) and $\delta = 1.0$ (rights).

By observing the phase diagrams on the μ-T plane, we can recognize the differences that emerge via the size of the system and the boundary conditions. In order to determine the size dependence of the chiral symmetry, we next plot the phase structure on a L-T plane. The phase diagrams on the L-T plane are shown in Figs. 4.5 ($D = 2$) and 4.6 ($D = 3$); the bottom figures are plotted at a larger size than the top figures. The finite size effect at $T = \mu = 0$ enhances the chiral symmetry breaking for the periodic boundary condition, and suppresses the symmetry breaking for the anti-periodic one [81]. However, it is also observed that these relations are reversed for certain intervals of size at a finite temperature and chemical potential. For low temperatures, the broken and the symmetric phases alternate with increasing size of the system, L.

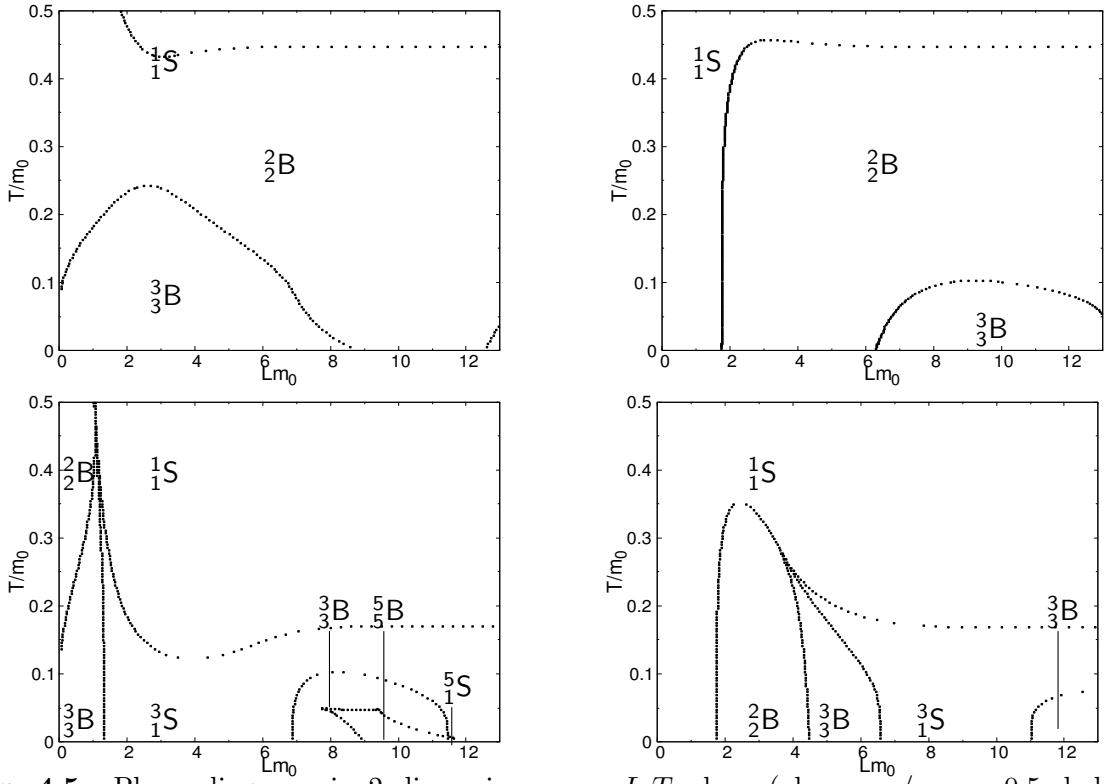

Fig. 4.5: Phase diagrams in 2 dimensions on a L-T plane (above: $\mu/m_0 = 0.5$, below: $\mu/m_0 = 0.7$) for $\delta = 0.0$ (lefts) and $\delta = 1.0$ (rights).

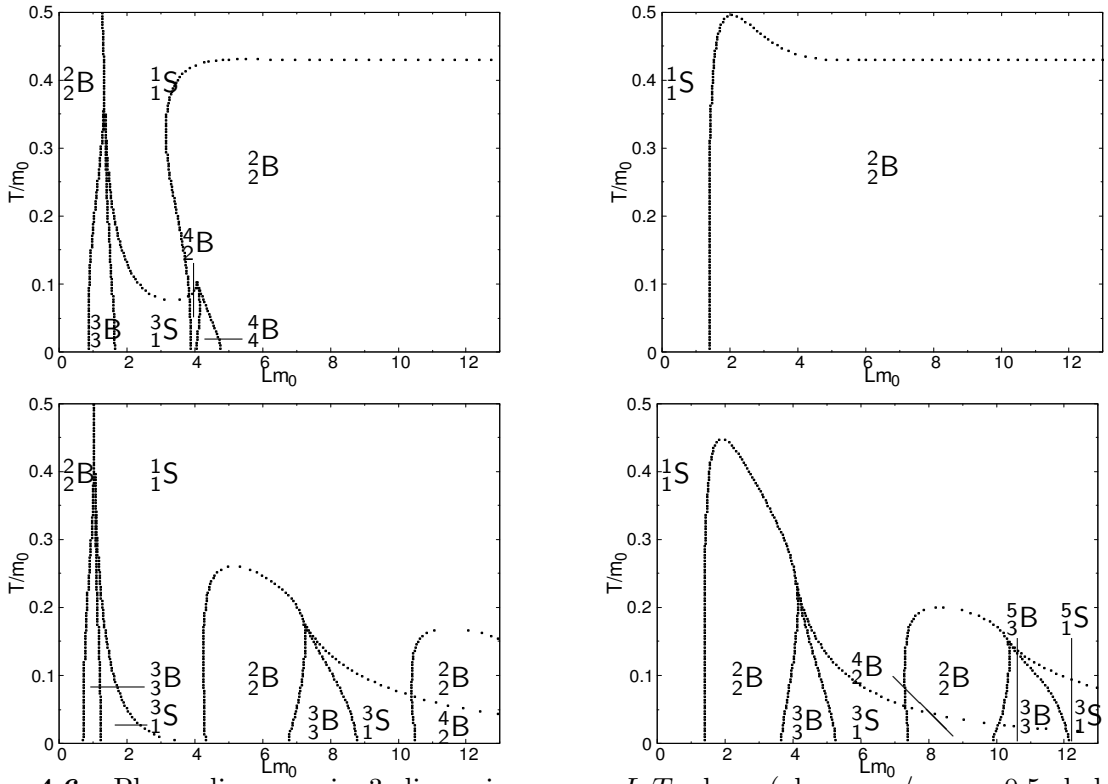

Fig. 4.6: Phase diagrams in 3 dimensions on a L-T plane (above: $\mu/m_0 = 0.5$, below: $\mu/m_0 = 0.7$) for $\delta = 0.0$ (lefts) and $\delta = 1.0$ (rights).

Dynamically generated fermion mass

The dynamically generated fermion mass, m, satisfies the gap equation,

$$\left.\frac{\partial V(\sigma; L, \delta, T, \mu)}{\partial \sigma}\right|_{\sigma=m} = 0. \tag{4.7}$$

We show the generated fermion mass as a function of the length of $\mathbb{S}^1$, L, and the U(1) phase, δ, in Figs. 4.7 ($D = 2$) and 4.8 ($D = 3$). The dashed black line ($m/m_0 = 1$) indicates the value in the trivial condition ($L \to \infty$, $T \to 0$ and $\mu = 0$). For $\mu = 0$ (purple lines) the generated fermion mass at $\delta = 0.0$ is heavier than that at $\delta = 1.0$. In the two graphs on the top of Figs. 4.7 and 4.8, the generated fermion mass vanishes and the chiral symmetry is restored around the periodic boundary condition ($\delta = 0.0$) slightly below the critical chemical potential.

This situation depends on the size, L. Observing the generated fermion mass as a function of L (green and yellow lines), we see that the broken and symmetric phases alternate with increasing length of $\mathbb{S}^1$, L. It is consistent with the phase diagrams, Figs. 4.5 and 4.6. The generated fermion mass changes more smoothly in three dimensions than in two dimensions, because of the continuous momentum.

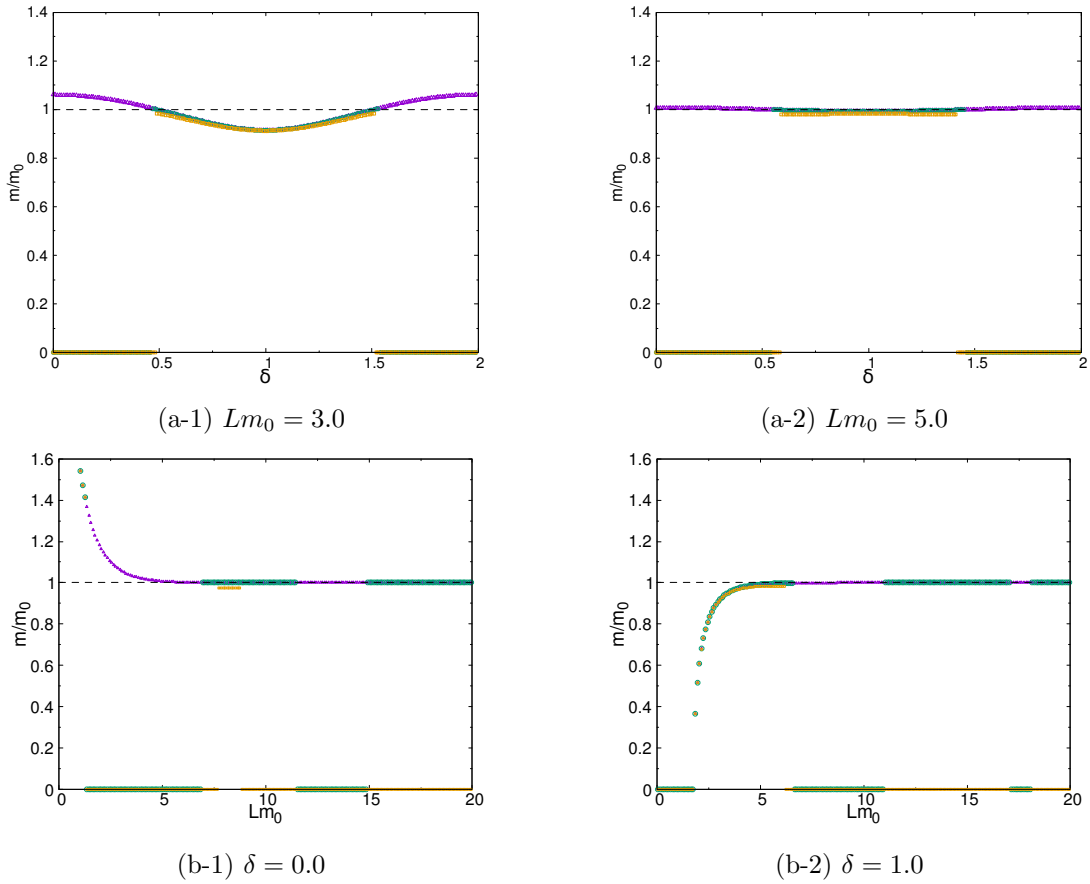

(a-1) $Lm_0 = 3.0$ (a-2) $Lm_0 = 5.0$

(b-1) $\delta = 0.0$ (b-2) $\delta = 1.0$

Fig. 4.7: Dynamically generated fermion mass as a function of δ (above) and L (below) in two dimensions: $(T/m_0, \mu/m_0; \text{color}) = (0.005, 0.0; \text{purple}),\ (0.005, 0.7; \text{green}),\ (0.1, 0.7; \text{yellow})$.

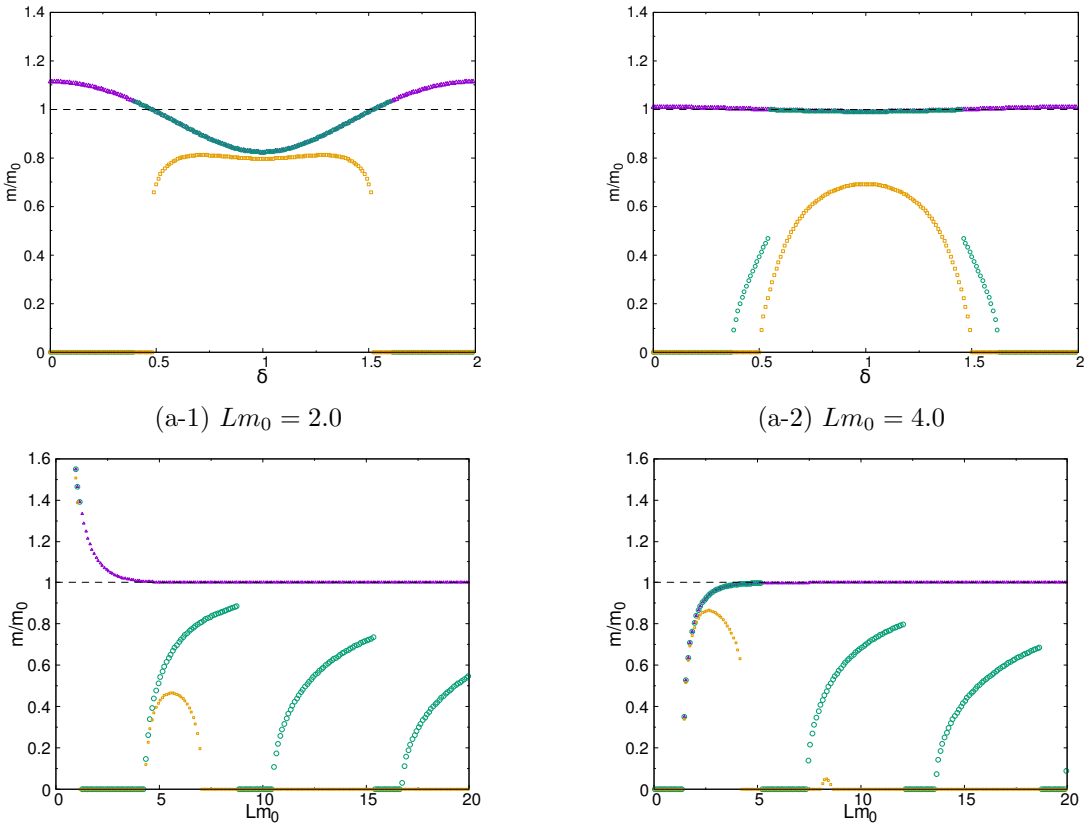

(a-1) $Lm_0 = 2.0$ (a-2) $Lm_0 = 4.0$

(b-1) $\delta = 0.0$ (b-2) $\delta = 1.0$

Fig. 4.8: Dynamically generated fermion mass as a function of δ (above) and L (below) in three dimensions: $(T/m_0, \mu/m_0; \text{color}) = (0.005, 0.0; \text{purple}), (0.005, 1.0; \text{green}), (0.2, 1.0; \text{yellow})$.

4.3 Thermodynamic Quantities

In Chapter 4.1 and 4.2, we have evaluated the effective potential and plotted the phase diagrams on the μ-T and L-T plane and the dynamically generated fermion mass. Other thermodynamic quantities are also derived from the effective potential. We here calculate and discuss particle number density and pressure.

Grand potential

A minimum value of the effective potential can be naively regarded as the density of the grand potential, denoted by $\Omega(L, \delta, T, \mu)$, as is mentioned at the last in Chapter 4.1. We set the value of the grand potential to zero in the trivial conditions: an infinite volume, zero temperature and zero chemical potential with a homogeneous and non-vanishing chiral condensate. The definition of the grand potential that wee consider is given by

$$\Omega(L, \delta, T, \mu) = V(m; L, \delta, T, \mu)L\mathcal{V} - V(m_0 L\mathcal{V}, \tag{4.8}$$

where $V(\sigma)$ denotes the effective potential on the trivial spacetime (derived in Chapter 2.2) and $L\mathcal{V}$ is $(D-1)$-dimensional volume.

The grand potential is shown in Figs. 4.9 ($D=2$) and 4.10 ($D=3$) as a function of the boundary condition, δ, and the length of $\mathbb{S}^1$, L. Bends of a line are observed at the same parameters at which the fermion mass jumps apper in Figs. 4.7 and 4.8. Thus, the phase boundary is found by observing the sharp bends if Figs. 4.9 and 4.10.

A stable size is a state for which the pressure is zero and becomes negative (positive) with increasing (decreasing) a length. We find the existence of a stable size for a finite chemical potential at a low temperature. For a finite chemical potential (green line), it is observed that the grand potential at $\delta = 0.0$ is minimized at $Lm_0 \sim 4.0$. This size is realized in the chirally symmetric phase. This stable state disappears at $\mu = 0$, because the grand potential (purple line) is a monotonic function of L and divergent at the small L limit.

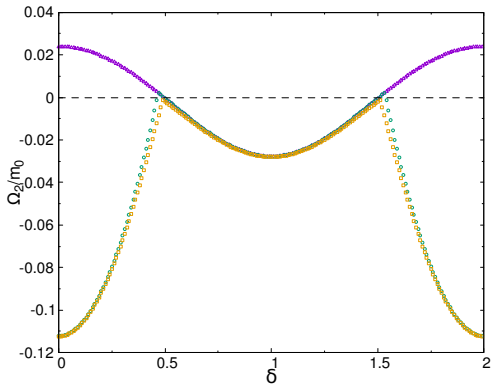

(a-1) $Lm_0 = 3.0$

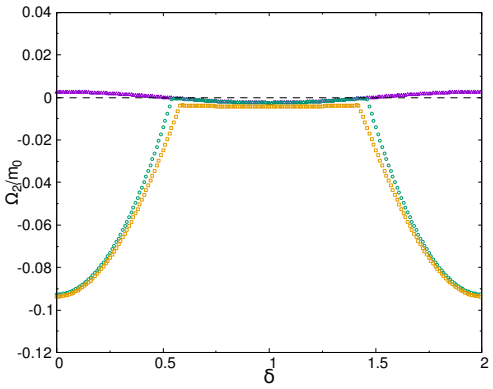

(a-2) $Lm_0 = 5.0$

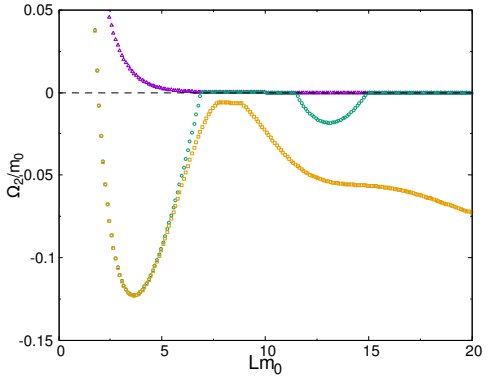

(b-1) $\delta = 0.0$

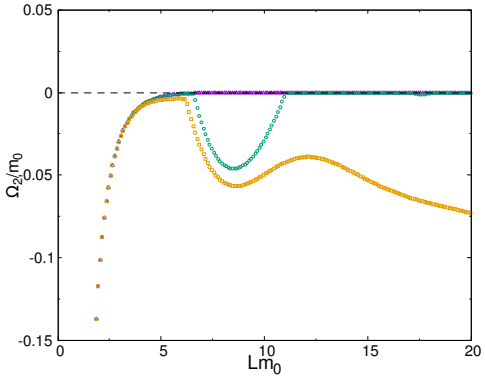

(b-2) $\delta = 1.0$

Fig. 4.9: Grand potential as a function of δ (above) and L (below) in two dimensions: $(T/m_0, \mu/m_0; \text{color}) = (0.005, 0.0; \text{purple}),\ (0.005, 0.7; \text{green}),\ (0.1, 0.7; \text{yellow})$.

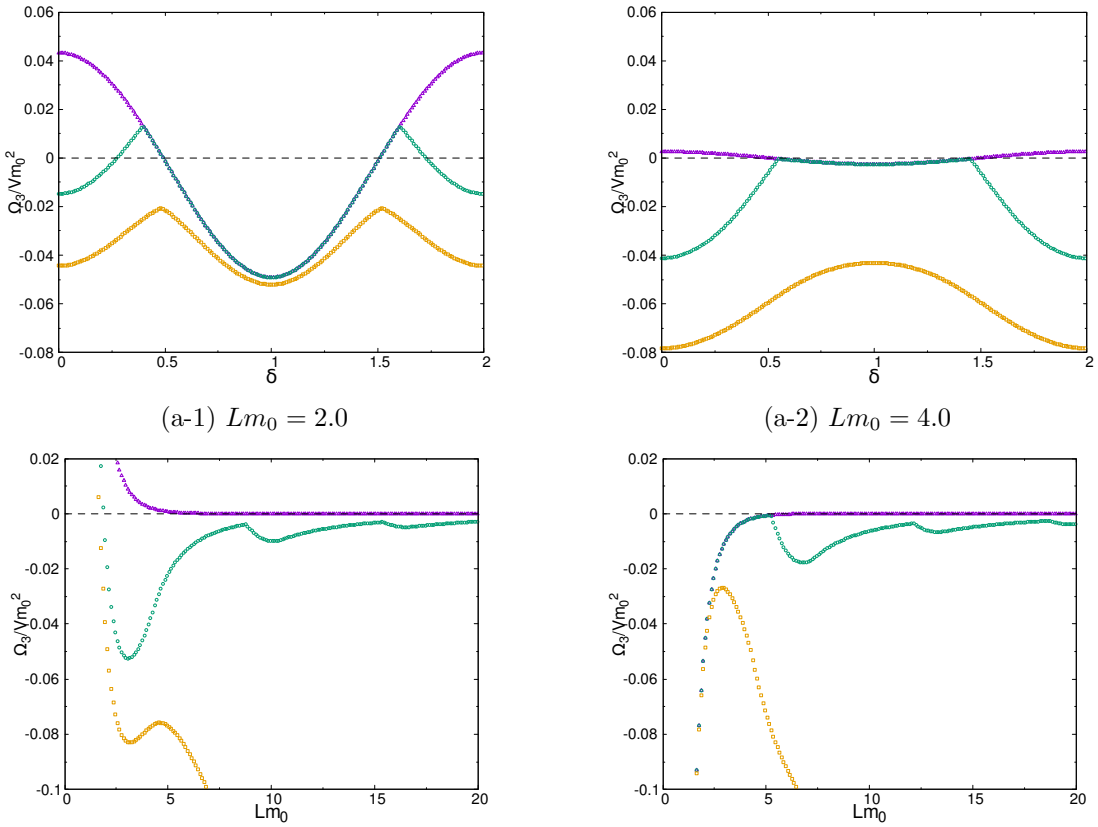

(a-1) $Lm_0 = 2.0$ (a-2) $Lm_0 = 4.0$

(b-1) $\delta = 0.0$ (b-2) $\delta = 1.0$

Fig. 4.10: Grand potential as a function of δ (above) and L (below) in three dimensions: $(T/m_0, \mu/m_0; \text{color}) = (0.005, 0.0; \text{purple}),\ (0.005, 1.0; \text{green}),\ (0.2, 1.0; \text{yellow})$.

Particle number density

To investigate the origin of the complex behavior of the phase diagrams, we study the contribution of the chemical potential. The particle number density is defined by the derivative of the grand potential with respect to the chemical potential,

$$\rho\left(L,\delta,T,\mu\right) = -\frac{1}{\mathcal{V}L}\frac{\partial\Omega\left(L,\delta,T,\mu\right)}{\partial\mu}. \tag{4.9}$$

The explicit expression normalized by m_0 is given by

$$\begin{aligned}&\frac{\rho\left(L,\delta,T,\mu\right)}{m_0^{D-1}}\\ =&\frac{\operatorname{tr} I}{\tilde{C}_D}\frac{1}{Lm_0}\sum_{n=-\infty}^{\infty}\int_0^\infty\frac{\mathrm{d}q}{m_0}\left(\frac{q}{m_0}\right)^{D-3}\frac{\sinh\mu/T}{\cosh\sqrt{q^2+k_{\delta,n}^2+m^2}/T+\cosh\mu/T}.\end{aligned}$$

For instance, the expression in two dimensions reads

$$\frac{\rho_2\left(L,\delta,T,\mu\right)}{m_0} = \frac{1}{Lm_0}\sum_{n=-\infty}^{\infty}\frac{\sinh\mu/T}{\cosh\sqrt{k_{\delta,n}^2+m^2}/T+\cosh\mu/T}. \tag{4.10}$$

We show the numerical results in Fig. 4.11 ($D = 2$)as a function of the boundary conditions, δ, and the length of $\mathbb{S}^1$, L. In the limit $T \to 0$, the each term of the sum is modified as

$$\frac{\sinh \mu/T}{\cosh \sqrt{k_{\delta,n}^2 + m^2}/T + \cosh \mu/T} \longrightarrow \mathrm{sgn}(\mu)\theta\left(|\mu| - \sqrt{k_{\delta,n}^2 + m^2}\right). \tag{4.11}$$

A non-zero lower bound appears for $k_{\delta,n}^2$, except for the periodic boundary condition. This implies that the particle number, $\rho_2(L, \delta, T, \mu)\, L$, takes an integer value at zero temperature. Because of the degeneracy of the states, the possible values are restricted to $0, 1, 3, 5, \ldots$ for $\delta = 0.0$ and $0, 2, 4, \ldots$ for $\delta = 1.0$. It is found that the correspondences between Figs. 4.7 (the generated fermion mass) and 4.11. The particle number density vanishes in the chiral broken phase for $m > 0$. In the symmetric phase, the particle number density vanishes because the non-zero lower bound for $k_{\delta=1.0,n}^2$ extremely suppresses the summation in Eq. (4.10) for $Lm_0 \lesssim 1.7$ at $\delta = 1.0$ (cf. the phase diagram in Chapter 3.2). At $T/m_0 = 0.1$, we observed pre-transitional phenomena because of the finite temperature effect.

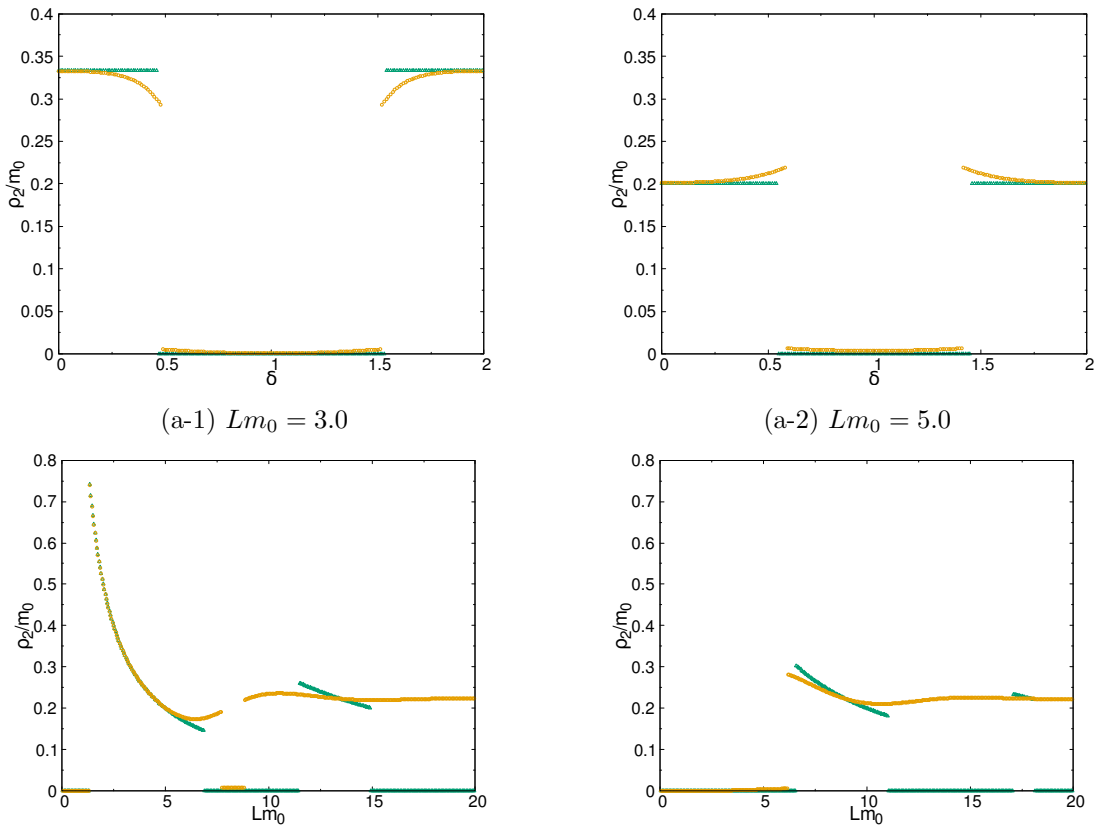

(a-1) $Lm_0 = 3.0$ (a-2) $Lm_0 = 5.0$

(b-1) $\delta = 0.0$ (b-2) $\delta = 1.0$

Fig. 4.11: Particle number density fixed to $\mu = 0.7$ as a function of δ (above) and L (below) in two dimensions. The green and yellow curve denotes $T/m_0 = 0.005$ and $T/m_0 = 0.1$ respectively.

As is shown in Fig. 4.12 ($D = 3$), the continuous momentum for the additional dimension

enhances the pre-transitional phenomena at a finite temperature and induces a finite number density near the phase boundary. Through the analysis of the particle number density and the comparison with the generated fermion mass, the complex behavior in the phase diagrams is caused by a balance between the particle production and the mass generation.

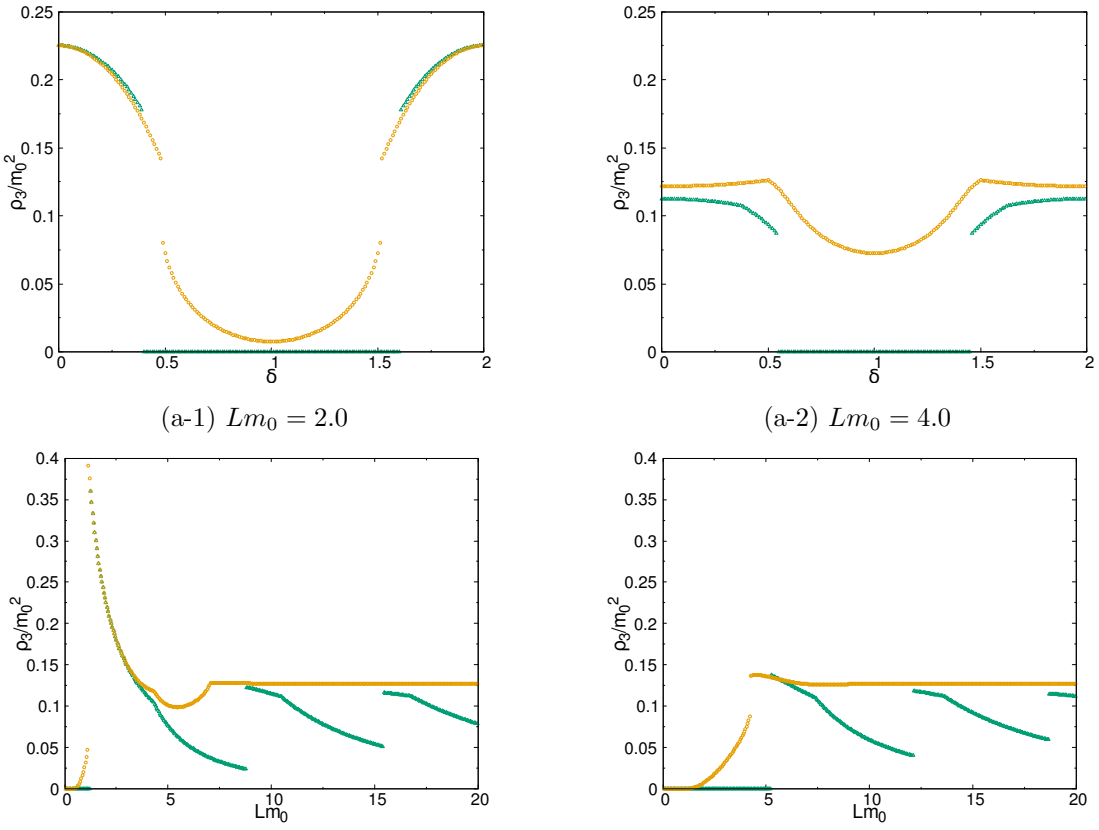

(a-1) $Lm_0 = 2.0$ (a-2) $Lm_0 = 4.0$

(b-1) $\delta = 0.0$ (b-2) $\delta = 1.0$

Fig. 4.12: Particle number density fixed to $\mu = 1.0$ as a function of δ (above) and L (below) in three dimensions. The green and yellow curve denotes $T/m_0 = 0.005$ and $T/m_0 = 0.2$ respectively.

Pressure

We have analyzed the particle number density and mentioned the correspondence between this quantity and the generated fermion mass in the preceding section. In order to find a stable size, we evaluated pressure. The pressure is defined by the derivative of the grand potential with respect to L,

$$P\left(L,\delta,T,\mu\right) = -\frac{1}{\mathcal{V}}\frac{\partial\Omega\left(L,\delta,T,\mu\right)}{\partial L}, \tag{4.12}$$

and explicitly expressed as

$$\begin{aligned}\frac{P\left(L,\delta,T,\mu\right)}{m_0^D} = &-\frac{\operatorname{tr} I\cdot\Gamma\left(1-\frac{D}{2}\right)}{(4\pi)^{\frac{D}{2}}}\left[\frac{1}{2}\left(\left(\frac{m}{m_0}\right)^2-1\right)-\frac{1}{D}\left(\left(\frac{m}{m_0}\right)^{2\cdot\frac{D}{2}}-1\right)\right]\\ &-\frac{\operatorname{tr} I}{C_D}\int_0^\infty\frac{\mathrm{d}q}{m_0}\left(\frac{q}{m_0}\right)^{D-2}\frac{\sqrt{q^2+m^2}}{m_0}\frac{\exp\left(-L\sqrt{q^2+m^2}\right)-\cos\pi\delta}{\cosh L\sqrt{q^2+m^2}-\cos\pi\delta}\\ &+\frac{\operatorname{tr} I}{\tilde{C}_D}\frac{1}{Lm_0}\sum_{n=-\infty}^{\infty}\int_0^\infty\frac{\mathrm{d}q}{m_0}\left(\frac{q}{m_0}\right)^{D-3}\\ &\qquad\times\frac{k_{\delta,n}^2}{m_0\sqrt{k_{\delta,n}^2+q^2+m^2}}\frac{\exp\left(-\sqrt{k_{\delta,n}^2+q^2+m^2}/T\right)+\cosh\mu/T}{\cosh\sqrt{k_{\delta,n}^2+q^2+m^2}/T+\cosh\mu/T}.\end{aligned}$$

In particular, the expression in two dimensions reads

$$\begin{aligned}\frac{P\left(L,\delta,T,\mu\right)}{m_0^2} = &-\frac{1}{4\pi}\left[1-\left(1-\ln\left(\frac{m}{m_0}\right)^2\right)\left(\frac{m}{m_0}\right)^2\right]\\ &-\frac{1}{\pi}\int_0^\infty\frac{\mathrm{d}q}{m_0}\frac{\sqrt{q^2+m^2}}{m_0}\frac{\exp\left(-L\sqrt{q^2+m^2}\right)-\cos\pi\delta}{\cosh L\sqrt{q^2+m^2}-\cos\pi\delta}\\ &+\frac{1}{Lm_0}\sum_{n=-\infty}^{\infty}\frac{k_{\delta,n}^2}{m_0\sqrt{k_{\delta,n}^2+m^2}}\frac{\exp\left(-\sqrt{k_{\delta,n}^2+m^2}/T\right)+\cosh\mu/T}{\cosh\sqrt{k_{\delta,n}^2+m^2}/T+\cosh\mu/T}.\end{aligned}$$

Behavior of the pressure as a function of the boundary conditions, δ, and the length of $\mathbb{S}^1$, L, is shown in Figs. 4.13 ($D=2$) and 4.14 ($D=3$). It is observed that, for a finite chemical potential, the jumps of the pressure are located at the same points where the generated fermion mass and the particle number density jump. As seen in Fig. 4.14 ($D=3$), one can finds the critical length, L, and U(1) phase, δ, for a second-order phase transition by observing the sharp bends of the pressure line.

With increasing the length, L, the finite-size effects are suppressed and the absolute value of the pressure tends to be smaller. At the same time, in particular $D=3$, it becomes apparent that the pressure is positively pushed up by thermal effects (the yellow lines on the below).

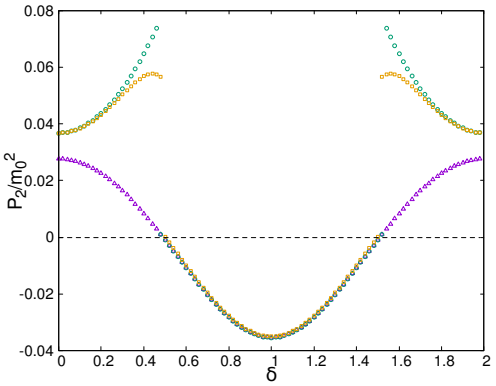

(a-1) $Lm_0 = 3.0$

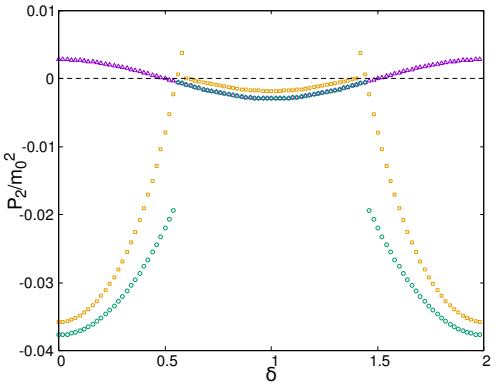

(a-2) $Lm_0 = 5.0$

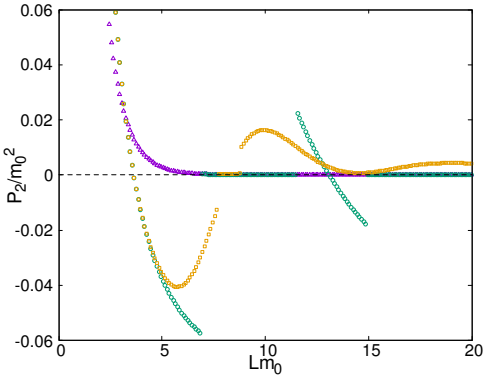

(b-1) $\delta = 0.0$

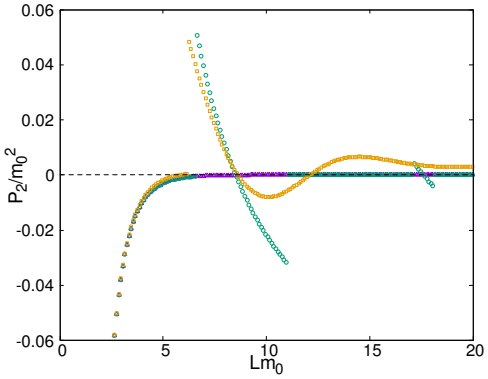

(b-2) $\delta = 1.0$

Fig. 4.13: Pressure as a function of δ (above) and L (below) in two dimensions. $(T/m_0, \mu/m_0; \text{color}) = (0.005, 0.0; \text{purple}),\ (0.005, 0.7; \text{green}),\ (0.1, 0.7; \text{yellow})$.

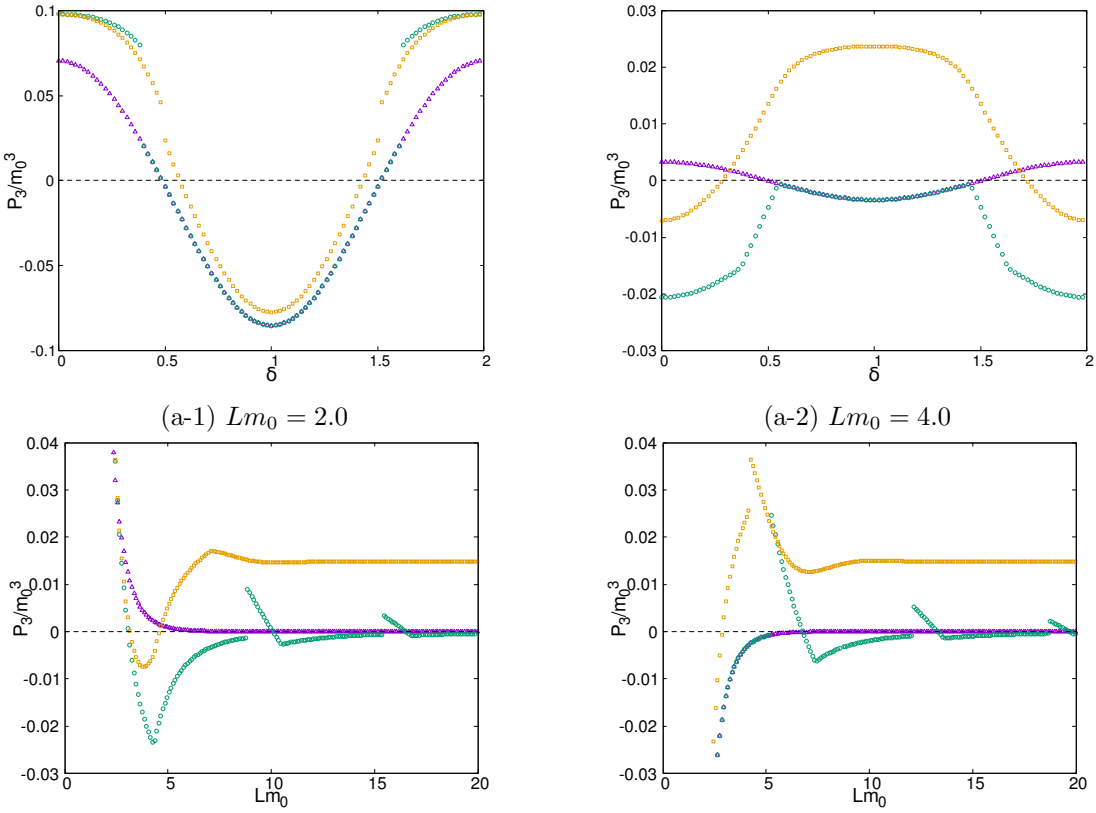

(a-1) $Lm_0 = 2.0$ (a-2) $Lm_0 = 4.0$

(b-1) $\delta = 0.0$ (b-2) $\delta = 1.0$

Fig. 4.14: Pressure as a function of δ (above) and L (below) in three dimensions. $(T/m_0, \mu/m_0; \text{color}) = (0.005, 0.0; \text{purple}),\ (0.005, 1.0; \text{green}),\ (0.2, 1.0; \text{yellow})$.

We call a size a stable size where the sign of the pressure flips from negative to positive as the size decreases. The sign-flip points of the pressure coincides with the local and global minima of the grand potential as a function of the length of $\mathbb{S}^1$, L. Figures 4.15 ($D = 2$) and 4.16 ($D = 3$) show behavior of the sigh-flip boundaries on a δ-L plane. A value of the chemical potential is distinguished by line colors: the purple line corresponds $\mu/m_0 = 0.0$ and the green lines correspond $\mu/m_0 = 0.7$ ($D = 2$) and $\mu/m_0 = 1.0$ ($D = 3$).

At a low temperature and zero chemical potential, denoted by the purple line on the left, the pressure is repulsive (attractive) near the (anti-)periodic boundary condition. Moreover, the sigh-flip boundary approaches $\delta = 0.5$, just the middle of the periodic and anti-periodic boundary conditions, with increasing the size. The finite-size effects are suppressed for a large size, L, and the thermal fluctuations induce a repulsive pressure. Thus, the repulsive pressure becomes favored for a large length, L, at higher temperatures, $T/m_0 = 0.1$ ($D = 2$; the right) and $T/m_0 = 0.2$ ($D = 3$; the right). The stable size at $\mu = 0$ can be found only for $Lm_0 \lesssim 1.0$ and $0.4 < \delta < 0.5$ in both the dimensions.

For a finite chemical potential denoted by green lines, one observes the complex behavior of the sign-flip boundaries on the δ-L plane. The stable size is found for a wider range of δ than at zero chemical potential. The size, for instance on the left in Fig. 4.15, exists on the

green lines at $Lm_0 \sim 4.0$ and $0 \leq \delta \lesssim 0.5$ and a metastable size at $Lm_0 \sim 7.0$ and $0.5 \lesssim \delta \leq 1$.

The second line of the effective potential (4.6) remains even at zero temperature and zero chemical potential, and thus describes the pure finite-size effect. For a small L, a dominant contribution to the potential energy comes from this term. For $1/2 < \delta \leq 1$, this term equivalent to the finite-size effect is negative and decreases the energy. As a result, an attractive pressure is induced. Whereas, the term is positive for $0 \leq \delta \leq 1/3$ and a repulsive pressure is induced. Thus, the sign of the pressure flips between $1/3 < \delta < 1/2$. As is read in the second line of the effective potential (4.6), Re $\left[\ln\left(1 + e^{-L\sqrt{q^2+\sigma^2}+i\pi\delta}\right)\right]$ is understood as an ansatz of the Bose–Einstein ($\delta = 0$) and Fermi–Dirac ($\delta = 1$) distributions in finite temperature systems. An opposite contribution to the thermodynamic potential is caused by this difference of the distributions. The U(1) phase, δ, is also regarded as an imaginary chemical potential [112, 113].

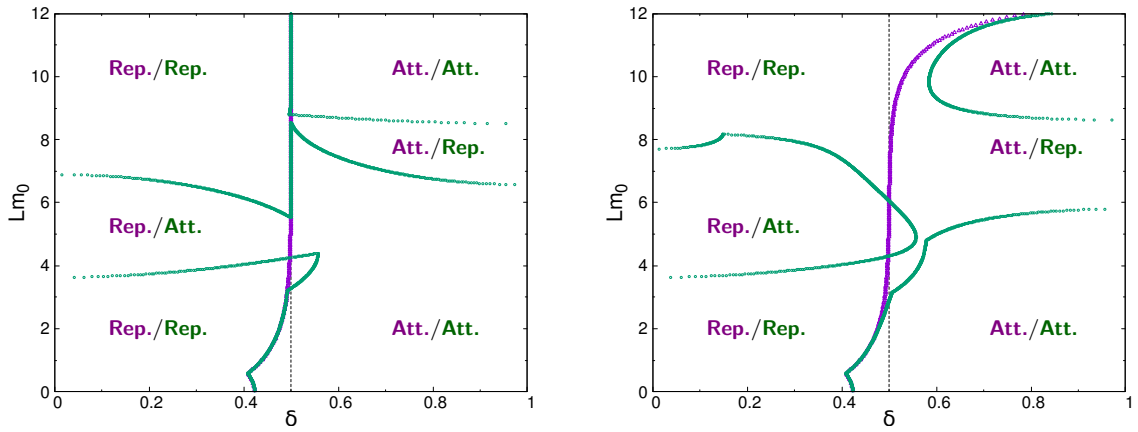

(a) $T/m_0 = 0.005$ (b) $T/m_0 = 0.1$

Fig. 4.15: Sign-flip boundaries of the pressure on the δ-L plane in two dimensions. The purple and green lines are $\mu/m_0 = 0.0$ and $\mu/m_0 = 1.0$, respectively. Xxx./Xxx. (Xxx. is Rep. or Att.) denotes whether the pressure is repulsive or attractive in the area at $\mu/m_0 = 0.0$ (left; purple) and $\mu/m_0 = 0.7$ (right; green).

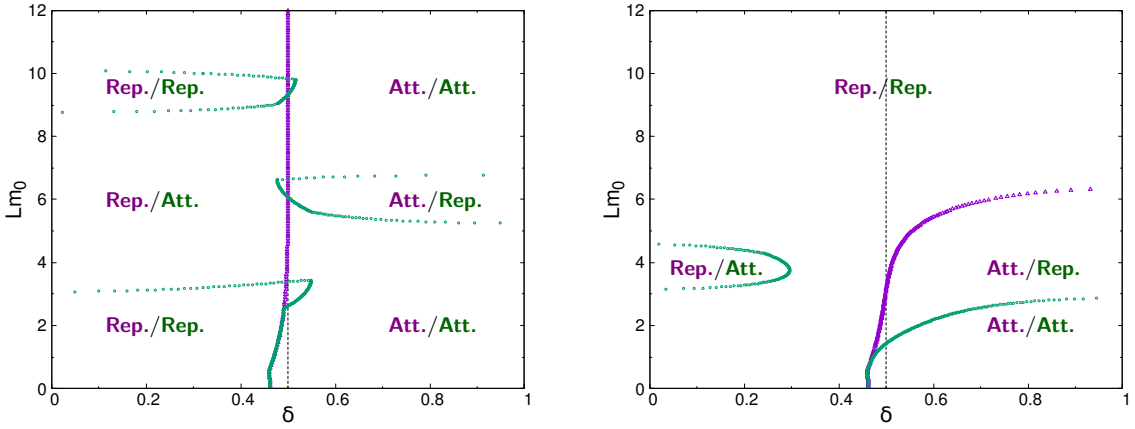

(a) $T/m_0 = 0.005$ (b) $T/m_0 = 0.2$

Fig. 4.16: Sign-flip boundaries of the pressure on the δ-L plane in three dimensions. The purple and green lines are $\mu/m_0 = 0.0$ and $\mu/m_0 = 1.0$, respectively. Xxx./Xxx. (Xxx. is Rep. or Att.) denotes whether the pressure is repulsive or attractive in the area at $\mu/m_0 = 0.0$ (left; purple) and $\mu/m_0 = 1.0$ (right; green).

Chapter 5

Summary and Discussions

Symmetry is a central concept in particle physics and the chiral symmetry is particularly important, albeit an approximate symmetry. Regardless of research fields, because the analysis from *ab initio* is often difficult in principle, investigation of the phase structure by using effective models is still significant, where the analysis with a wide range of parameters is necessary. In this thesis, employing the four-fermion interaction model called the Gross–Neveu model, we have evaluated the effective potential in the leading order of the $1/N$ expansion in order to investigate the phase structure in terms of the chiral symmetry. The effective potential is derived with supposing a homogeneous chiral condensate. To study the finite-size effect in addition to the thermal effect with chemical potential, we have compactified a spacial direction to a one-dimensional sphere, $\mathbb{S}^1$, and besides imposed the U(1)-valued boundary condition to the fermion.

In Chapter 3, we have considered the finite-size effect at zero temperature. We have derived the improved effective potential compared with [50] paying attention to the finite part of the subtraction of the divergence. The subtraction before our improvement includes the parameters of the finite-size effect, L and δ, and hence prevents the correspondence between the effective potential and the phase of the grand state. The chiral symmetry breaking tends to be enhanced at the periodic boundary condition, $\delta = 0$. On the contrary, the anti-periodic boundary condition, $\delta = 1$, shows opposite results for the chiral symmetry. This behavior becomes clear with decreasing the size of $\mathbb{S}^1$. The system with the anti-periodic boundary condition can be regarded to mimic the finite temperature system filled with the fermions. The phase transitions can be detected by the sharp bends on the lines of the dynamically generated fermion mass and string tension. We have found sign-flip boundaries of the string tension in the restricted region, $0.4 < \delta < 0.5$, for any finite size. At zero temperature, it seems difficult to keep the system at a finite size.

In Chapter 4, we have extended the study on Chapter 3 and considered the finite-size effect with a finite temperature and a finite chemical potential. In order to investigate the phase structure more precisely, we have evaluated the effective potential by observing not only the minimum but also the extrema. We have found the boundaries at which the number of the

extrema and the position of the minimum change on the μ-T and L-T planes. The finite-size effect induces the complex structure at a low temperature and a high chemical potential on the μ-T plane. Observing the L-T plane, the broken and the symmetric phases alternate with increasing the size of $\mathbb{S}^1$. We also have shown this behavior of the generated fermion mass as a function of L and δ. By using the grand potential defined as the zero-point is located at $L \to \infty$, $T \to 0$ and $\mu = 0$, we have found the stable size for a finite chemical potential near the periodic boundary condition. Through the analysis of the particle number density, the trade-off relationship between the generated fermion mass and the particle number density is shown. The jumps of the mass and density take place at the same L and δ. Based on the analysis of the thermodynamic quantities, it is considered that the complex behavior of the boundaries on the phase diagrams is caused by the competition among the generated fermion mass, the inverse of the size, $2\pi/L$, and the chemical potential. Alternatively, the sign-flip boundaries gives us information about the stable and metastable sizes. It is found that the sizes additionally appear caused by the contribution of a finite chemical potential.

We have discussed the finite-size effect in the Gross–Neveu model and shown this effect on the phase structure along with thermodynamic quantities in terms of the chiral symmetry. However, we have analyzed only the one-dimensional sphere $\mathbb{S}^1$. There are many shapes of systems with various topologies. On the other hand, to consider more realistic situations, it is necessary to introduce fermion mass, fermion flavors, and an electromagnetic field. Recently, the inhomogeneous chiral condensate are theoretically discussed. The works relatively close to our study, as is already mentioned in Chapter 1 and Chapter 4.2, the Fulde–Ferrell–Larkin–Ovchinnikov states are discussed in a superconducting ring with magnetic flux [54]. Furthermore, it is also pointed out that the possibility of the inhomogeneous chiral condensate can not be ignored in a finite-size system [56]. In Ref. [114], the inhomogeneous chiral condensate are investigated by using lattice simulations.

Appendix A

Notation

In this thesis, we adopt Planck units,

$$\hbar = c = k_{\mathrm{B}} = 1, \tag{A.1}$$

and diag$(+,-,-,-)$ as a metric signature on a Minkowski spacetime, $\mathcal{M}^4$. Extending the metric signature, we also use diag$(+,-,\ldots,-)$ on a D-dimensional Minkowski spacetime, $\mathcal{M}^D$. The metric is denoted by $\eta_{\mu\nu}$ and $\eta^{\mu\nu}$. The sign of the zeroth component, the temporal component, is positive and the others, the spatial components, are negative.

Greek indices, such as $\mu, \nu, \rho, \ldots$, run from 0 to $D-1$, and Latin indices, such as $i, j, k, \ldots$, from 1 to D. When an index variable appears as upper and lower indices in a term, it implies a summation over all a range of index variables: $x^\mu p_\mu = x^0 p_0 + \cdots + x^{D-1} p_{D-1}$ and $k^j k_j = k^1 k_1 + \cdots + k^D k_D$. We use a bold font to describe a quantity without a zeroth (or temporal) component, such as $\boldsymbol{k^2} = k_1^2 + \cdots + k_3^2$ and $\boldsymbol{p^2} = p_1^2 + \cdots + p_4^2$.

A set of gamma matrices, $\gamma^\mu\,(\mu = 0, 1, \ldots, D-1)$, is a basis of the Clifford algebra, a space of spinors, that satisfies

$$\{\gamma^\mu, \gamma^\nu\} = \gamma^\mu\gamma^\nu + \gamma^\nu\gamma^\mu = 2\eta^{\mu\nu} I, \tag{A.2}$$

with I denoting an identity matrix in the spinor space. γ^5 is a chiral operator that satisfies

$$\{\gamma^5, \gamma^\mu\} = 0. \tag{A.3}$$

Acknowledgements

I would like to thank Prof. Tomohiro Inagaki, as a supervisor and coauthor, for valuable and helpful discussions and advise. Also I would like to thank Prof. Daiji Kimura, Dr. Hiroki Sakamoto and Dr. Yamato Matsuo for fruitful discussions. I am grateful to staff and colleagues in the laboratory. Finally, I give special thanks to my parents, Hiroaki and Akemi, for their great supports.

Bibliography

[1] J. Bardeen, L. N. Cooper, and J. R. Schrieffer, Phys. Rev. **106** (1957) 162, doi:10.1103/PhysRev.106.162.

[2] Y. Nambu and G. Jona-Lasinio, Phys. Rev. **122** (1961) 345–358, doi:10.1103/PhysRev.122.345.

[3] Y. Nambu and G. Jona-Lasinio, Phys. Rev. **124** (1961) 246–254, doi:10.1103/PhysRev.124.246.

[4] D. J. Gross and F. Wilczek, Phys. Rev. Lett. **30** (1973) 1343–1346, doi:10.1103/PhysRevLett.30.1343.

[5] H. D. Politzer, Phys. Rev. Lett. **30** (1973) 1346–1349, doi:10.1103/PhysRevLett.30.1346.

[6] S. Muroya, A. Nakamura, C. Nonaka, and T. Takaishi, Prog. Theor. Phys. **110** (2003) 615–668, doi:10.1143/PTP.110.615, arXiv:hep-lat/0306031.

[7] P. de Forcrand, PoS **LAT2009** (2009) 010, doi:10.22323/1.091.0010, arXiv:1005.0539 [hep-lat].

[8] C. R. Allton, S. Ejiri, S. J. Hands, O. Kaczmarek, F. Karsch, E. Laermann, C. Schmidt, and L. Scorzato, Phys. Rev. D **66** (2002) 074507, doi:10.1103/PhysRevD.66.074507, arXiv:hep-lat/0204010.

[9] **WHOT-QCD** Collaboration, S. Ejiri, Y. Maezawa, N. Ukita, S. Aoki, T. Hatsuda, N. Ishii, K. Kanaya, and T. Umeda, Phys. Rev. D **82** (2010) 014508, doi:10.1103/PhysRevD.82.014508, arXiv:0909.2121 [hep-lat].

[10] M. G. Alford, A. Kapustin, and F. Wilczek, Phys. Rev. D **59** (1999) 054502, doi:10.1103/PhysRevD.59.054502, arXiv:hep-lat/9807039.

[11] P. de Forcrand and O. Philipsen, Nucl. Phys. B **642** (2002) 290–306, doi:10.1016/S0550-3213(02)00626-0, arXiv:hep-lat/0205016.

[12] P. de Forcrand and O. Philipsen, Nucl. Phys. B **673** (2003) 170–186, doi:10.1016/j.nuclphysb.2003.09.005, arXiv:hep-lat/0307020.

[13] P. de Forcrand and O. Philipsen, Phys. Rev. Lett. **105** (2010) 152001, doi:10.1103/PhysRevLett.105.152001, arXiv:1004.3144 [hep-lat].

[14] K. Nagata and A. Nakamura, Phys. Rev. D **83** (2011) 114507, doi:10.1103/PhysRevD.83.114507, arXiv:1104.2142 [hep-lat].

[15] G. Aarts, Phys. Rev. Lett. **102** (2009) 131601, doi:10.1103/PhysRevLett.102.131601, arXiv:0810.2089 [hep-lat].

[16] G. Aarts, L. Bongiovanni, E. Seiler, D. Sexty, and I.-O. Stamatescu, Eur. Phys. J. A **49** (2013) 89, doi:10.1140/epja/i2013-13089-4, arXiv:1303.6425 [hep-lat].

[17] D. Sexty, Phys. Lett. B **729** (2014) 108–111, doi:10.1016/j.physletb.2014.01.019, arXiv:1307.7748 [hep-lat].

[18] J. Nishimura and S. Shimasaki, Phys. Rev. D **92** (2015) no. 1, 011501, doi:10.1103/PhysRevD.92.011501, arXiv:1504.08359 [hep-lat].

[19] K. Nagata, J. Nishimura, and S. Shimasaki, Phys. Rev. D **94** (2016) no. 11, 114515, doi:10.1103/PhysRevD.94.114515, arXiv:1606.07627 [hep-lat].

[20] **AuroraScience** Collaboration, M. Cristoforetti, F. Di Renzo, and L. Scorzato, Phys. Rev. D **86** (2012) 074506, doi:10.1103/PhysRevD.86.074506, arXiv:1205.3996 [hep-lat].

[21] H. Fujii, D. Honda, M. Kato, Y. Kikukawa, S. Komatsu, and T. Sano, JHEP **10** (2013) 147, doi:10.1007/JHEP10(2013)147, arXiv:1309.4371 [hep-lat].

[22] M. Levin and C. P. Nave, Phys. Rev. Lett. **99** (2007) no. 12, 120601, doi:10.1103/PhysRevLett.99.120601, arXiv:cond-mat/0611687.

[23] Z. Y. Xie, J. Chen, M. P. Qin, J. W. Zhu, L. P. Yang, and T. Xiang, Physical Review B **86** (Jul, 2012) no. 4, , doi:10.1103/physrevb.86.045139. https://doi.org/10.1103%2Fphysrevb.86.045139.

[24] S. Akiyama, D. Kadoh, Y. Kuramashi, T. Yamashita, and Y. Yoshimura, JHEP **09** (2020) 177, doi:10.1007/JHEP09(2020)177, arXiv:2005.04645 [hep-lat].

[25] S. Akiyama, Y. Kuramashi, T. Yamashita, and Y. Yoshimura, JHEP **01** (2021) 121, doi:10.1007/JHEP01(2021)121, arXiv:2009.11583 [hep-lat].

[26] J. B. Kogut, M. A. Stephanov, D. Toublan, J. J. M. Verbaarschot, and A. Zhitnitsky, Nucl. Phys. B **582** (2000) 477–513, doi:10.1016/S0550-3213(00)00242-X, arXiv:hep-ph/0001171.

[27] S. Klevansky, Rev. Mod. Phys. **64** (1992) 649–708, doi:10.1103/RevModPhys.64.649.

[28] T. Hatsuda and T. Kunihiro, Phys. Rept. **247** (1994) 221–367, doi:10.1016/0370-1573(94)90022-1, arXiv:hep-ph/9401310.

[29] D. J. Gross and A. Neveu, Phys. Rev. **D10** (1974) 3235, doi:10.1103/PhysRevD.10.3235.

[30] D. Kahana and U. Vogl, Phys. Lett. B **244** (1990) 10–18, doi:10.1016/0370-2693(90)90260-D.

[31] D. Ebert, L. Kaschluhn, and G. Kastelewicz, Phys. Lett. B **264** (1991) 420–425, doi:10.1016/0370-2693(91)90371-V.

[32] K. Fukushima, Phys. Lett. B **591** (2004) 277–284, doi:10.1016/j.physletb.2004.04.027, arXiv:hep-ph/0310121.

[33] B. Rosenstein, B. Warr, and S. Park, Phys. Rept. **205** (1991) 59–108, doi:10.1016/0370-1573(91)90129-A.

[34] T. Inagaki, T. Muta, and S. D. Odintsov, Prog. Theor. Phys. Suppl. **127** (1997) 93, doi:10.1143/PTPS.127.93, arXiv:hep-th/9711084 [hep-th].

[35] V. A. Miransky and I. A. Shovkovy, Phys. Rept. **576** (2015) 1–209, doi:10.1016/j.physrep.2015.02.003, arXiv:1503.00732 [hep-ph].

[36] K. Hattori and X.-G. Huang, Nucl. Sci. Tech. **28** (2017) no. 2, 26, doi:10.1007/s41365-016-0178-3, arXiv:1609.00747 [nucl-th].

[37] Y. Jiang and J. Liao, Phys. Rev. Lett. **117** (2016) no. 19, 192302, doi:10.1103/PhysRevLett.117.192302, arXiv:1606.03808 [hep-ph].

[38] K. Fukushima, Prog. Part. Nucl. Phys. **107** (2019) 167–199, doi:10.1016/j.ppnp.2019.04.001, arXiv:1812.08886 [hep-ph].

[39] V. P. Gusynin, V. A. Miransky, and I. A. Shovkovy, Phys. Lett. B **349** (1995) 477–483, doi:10.1016/0370-2693(95)00232-A, arXiv:hep-ph/9412257.

[40] V. P. Gusynin, V. A. Miransky, and I. A. Shovkovy, Nucl. Phys. B **462** (1996) 249–290, doi:10.1016/0550-3213(96)00021-1, arXiv:hep-ph/9509320.

[41] M. N. Chernodub and S. Gongyo, Phys. Rev. D **95** (2017) no. 9, 096006, doi:10.1103/PhysRevD.95.096006, arXiv:1702.08266 [hep-th].

[42] S. K. Kim, W. Namgung, K. S. Soh, and J. H. Yee, Phys. Rev. **D36** (1987) 3172–3177, doi:10.1103/PhysRevD.36.3172.

[43] K. Ishikawa, T. Inagaki, K. Yamamoto, and K. Fukazawa, Prog. Theor. Phys. **99** (1998) 237–255, doi:10.1143/PTP.99.237.

[44] A. V. Gamayun and E. V. Gorbar, Phys. Lett. B **610** (2005) 74–79, doi:10.1016/j.physletb.2005.01.079, arXiv:hep-ph/0411157.

[45] D. Ebert and K. G. Klimenko, Phys. Rev. D **82** (2010) 025018, doi:10.1103/PhysRevD.82.025018, arXiv:1005.0699 [hep-ph].

[46] L. M. Abreu and E. S. Nery, Phys. Rev. C **96** (2017) no. 5, 055204, doi:10.1103/PhysRevC.96.055204, arXiv:1711.07934 [nucl-th].

[47] T. Ishikawa, K. Nakayama, and K. Suzuki, Phys. Lett. B **809** (2020) 135713, doi:10.1016/j.physletb.2020.135713, arXiv:2005.10758 [hep-lat].

[48] T. Ishikawa, K. Nakayama, and K. Suzuki, Phys. Rev. Res. **3** (2021) no. 2, 023201, doi:10.1103/PhysRevResearch.3.023201, arXiv:2012.11398 [hep-lat].

[49] A. Higuchi and L. Parker, Phys. Rev. **D37** (1988) 2853–2871, doi:10.1103/PhysRevD.37.2853.

[50] S. Huang and B. Schreiber, Nucl. Phys. B **426** (1994) no. 3, 644–660, doi:10.1016/0550-3213(94)90024-8, arXiv:cond-mat/9404080 [cond-mat].

[51] D. Y. Song, Phys. Rev. **D48** (1993) 3925–3928, doi:10.1103/PhysRevD.48.3925.

[52] A. Flachi, Phys. Rev. D **88** (2013) no. 4, 041501, doi:10.1103/PhysRevD.88.041501, arXiv:1305.5348 [hep-th].

[53] A. Flachi, Phys. Rev. D **88** (2013) no. 8, 085011, doi:10.1103/PhysRevD.88.085011, arXiv:1304.6880 [hep-th].

[54] R. Yoshii, S. Takada, S. Tsuchiya, G. Marmorini, H. Hayakawa, and M. Nitta, Phys. Rev. **B92** (2015) no. 22, 224512, doi:10.1103/PhysRevB.92.224512, arXiv:1404.3519 [cond-mat.supr-con].

[55] Y. Aharonov and D. Bohm, Phys. Rev. **115** (1959) 485–491, doi:10.1103/PhysRev.115.485.

[56] A. Flachi, Phys. Rev. D **86** (2012) 104047, doi:10.1103/PhysRevD.86.104047, arXiv:1209.4754 [hep-th].

[57] H. B. G. Casimir and D. Polder, Phys. Rev. **73** (1948) 360–372, doi:10.1103/PhysRev.73.360.

[58] H. Casimir, Proc. Kon. Ned. Akad. Wetensch. **51** (1948) 793–795.

[59] K. A. Milton, L. L. DeRaad, Jr., and J. S. Schwinger, Annals Phys. **115** (1978) 388, doi:10.1016/0003-4916(78)90161-6.

[60] K. A. Milton, Annals Phys. **127** (1980) 49, doi:10.1016/0003-4916(80)90149-9.

[61] I. Brevik, Annals Phys. **138** (1982) no. 1, 36–52, doi:https://doi.org/10.1016/0003-4916(82)90174-9.

[62] I. Brevik and H. Kolbenstvedt, Annals Phys. **143** (1982) no. 1, 179–190, doi:https://doi.org/10.1016/0003-4916(82)90218-4.

[63] G. Plunien, B. Müller, and W. Greiner, Phys. Rept. **134** (1986) no. 2, 87–193, doi:https://doi.org/10.1016/0370-1573(86)90020-7.

[64] M. Bordag, E. Elizalde, and K. Kirsten, J. Math. Phys. **37** (1996) 895–916, doi:10.1063/1.531418, arXiv:hep-th/9503023.

[65] E. Elizalde, L. Vanzo, and S. Zerbini, Commun. Math. Phys. **194** (1998) 613–630, doi:10.1007/s002200050371, arXiv:hep-th/9701060.

[66] M. Bordag, U. Mohideen, and V. M. Mostepanenko, Phys. Rept. **353** (2001) 1–205, doi:10.1016/S0370-1573(01)00015-1, arXiv:quant-ph/0106045.

[67] K. A. Milton, *"The Casimir Effect: Physical Manifestations of Zero-Point Energy"*, World Scientific, Hackensack, NJ, US, 2001.

[68] M. Bordag, G. L. Klimchitskaya, U. Mohideen, and V. M. Mostepanenko, *"Advances in the Casimir Effect"*, Oxford University Press, Oxford, UK, 2009.

[69] D. Dalvit, P. Milonni, D. Roberts, and F. Rosa, *"Casimir Physics"*, Springer, Berlin, Germany, 2011.

[70] W. M. R. Simpson and U. Leonhardt, *"Forces fo the Quantum Vacuum: An Introduction to Casimir Physics"*, World Scientific, Hackensack, NJ, US, 2015.

[71] I. E. Dzyaloshinskii, E. M. Lifshitz, and L. P. Pitaevskii, Advances in Physics **10** (1961) no. 38, 165–209, doi:10.1080/00018736100101281.

[72] T. H. Boyer, Phys. Rev. **174** (1968) 1764–1774, doi:10.1103/PhysRev.174.1764.

[73] T. H. Boyer, Phys. Rev. A **9** (1974) 2078–2084, doi:10.1103/PhysRevA.9.2078.

[74] S. Rode, R. Bennett, and S. Y. Buhmann, New J. Phys. **20** (2018) no. 4, 043024, doi:10.1088/1367-2630/aaaa44, arXiv:1710.01509 [quant-ph].

[75] A. Flachi, Phys. Rev. Lett. **110** (2013) no. 6, 060401, doi:10.1103/PhysRevLett.110.060401, arXiv:1301.1193 [hep-th].

[76] A. Flachi, M. Nitta, S. Takada, and R. Yoshii, Phys. Rev. Lett. **119** (2017) no. 3, 031601, doi:10.1103/PhysRevLett.119.031601, arXiv:1704.04918 [hep-th].

[77] M. Nitta and R. Yoshii, JHEP **12** (2017) 145, doi:10.1007/JHEP12(2017)145, arXiv:1707.03207 [hep-th].

[78] M. N. Chernodub, V. A. Goy, and A. V. Molochkov, Phys. Rev. D **99** (2019) no. 7, 074021, doi:10.1103/PhysRevD.99.074021, arXiv:1811.01550 [hep-lat].

[79] M. N. Chernodub, V. A. Goy, and A. V. Molochkov, PoS **Confinement2018** (2019) 006, doi:10.22323/1.336.0006, arXiv:1901.04754 [hep-th].

[80] T. Ishikawa, K. Nakayama, D. Suenaga, and K. Suzuki, Phys. Rev. D **100** (2019) no. 3, 034016, doi:10.1103/PhysRevD.100.034016, arXiv:1905.11164 [hep-ph].

[81] T. Inagaki, Y. Matsuo, and H. Shimoji, Symmetry **11** (2019) no. 4, 451, doi:10.3390/sym11040451, arXiv:1903.04244 [hep-th].

[82] T. Inagaki, Y. Matsuo, and H. Shimoji, PTEP **2022** (2022) no. 1, 013B09, doi:10.1093/ptep/ptab160, arXiv:2108.03583 [hep-ph].

[83] R. L. Stratonovich, Soviet Physics Doklady **2** (1957) 416.

[84] J. Hubbard, Phys. Rev. Lett. **3** (1959) 77–78, doi:10.1103/PhysRevLett.3.77.

[85] T. Kashiwa and T. Sakaguchi, Phys. Rev. D **68** (2003) 065002, doi:10.1103/PhysRevD.68.065002, arXiv:hep-th/0306008.

[86] H. Kohyama, D. Kimura, and T. Inagaki, Nucl. Phys. B **896** (2015) 682–715, doi:10.1016/j.nuclphysb.2015.05.015, arXiv:1501.00449 [hep-ph].

[87] H. Kohyama, D. Kimura, and T. Inagaki, Nucl. Phys. B **906** (2016) 524–548, doi:10.1016/j.nuclphysb.2016.03.015, arXiv:1601.02411 [hep-ph].

[88] J. S. Schwinger, Phys. Rev. **82** (1951) 664–679, doi:10.1103/PhysRev.82.664.

[89] C. Itzykson and J. Zuber, *"Quantum Field Theory"*, McGrow-Hill, New York, USA, 1980.

[90] E. Elizalde and S. D. Sergei, Odintsov, *"Zeta regularization Techniques with Applications"*, World Scientific, Singapore, 1994.

[91] E. Elizalde, *"Ten Physical Applications of Spectral Zeta Functions"*, Springer, Berlin, Germany, 2012.

[92] N. D. Mermin and H. Wagner, Phys. Rev. Lett. **17** (1966) 1133–1136, doi:10.1103/PhysRevLett.17.1133.

[93] P. C. Hohenberg, Phys. Rev. **158** (1967) 383–386, doi:10.1103/PhysRev.158.383.

[94] S. R. Coleman, Commun. Math. Phys. **31** (1973) 259–264, doi:10.1007/BF01646487.

[95] T. Fujihara, T. Inagaki, and D. Kimura, J. Phys. A **39** (2006) 6371–6376, doi:10.1088/0305-4470/39/21/S30, arXiv:hep-ph/0511286.

[96] T. Inagaki, D. Kimura, and A. Kvinikhidze, Phys. Rev. D **77** (2008) 116004, doi:10.1103/PhysRevD.77.116004, arXiv:0712.1336 [hep-ph].

[97] T. Fujihara, T. Inagaki, D. Kimura, and A. Kvinikhidze, Prog. Theor. Phys. Suppl. **174** (2008) 72–75, doi:10.1143/PTPS.174.72, arXiv:0806.1331 [hep-ph].

[98] T. Inagaki, D. Kimura, H. Kohyama, and A. Kvinikhidze, Phys. Rev. D **83** (2011) 034005, doi:10.1103/PhysRevD.83.034005, arXiv:1010.0309 [hep-ph].

[99] T. Eguchi, Phys. Rev. D **17** (1978) 611, doi:10.1103/PhysRevD.17.611.

[100] K.-i. Shizuya, Phys. Rev. D **21** (1980) 2327, doi:10.1103/PhysRevD.21.2327.

[101] S. Aoki and K. Higashijima, Prog. Theor. Phys. **76** (1986) 521, doi:10.1143/PTP.76.521.

[102] D. Ebert and K. G. Klimenko, Phys. Rev. D **80** (2009) 125013, doi:10.1103/PhysRevD.80.125013, arXiv:0911.1944 [hep-ph].

[103] T. Matsubara, Prog. Theor. Phys. **14** (1955) 351–378, doi:10.1143/PTP.14.351.

[104] H. Ezawa, Y. Tomozawa, and H. Umezawa, Nuovo Cim. **5** (1957) 810–841, doi:10.1007/BF02903206.

[105] L. Dolan and R. Jackiw, Phys. Rev. D **9** (1974) 3320–3341, doi:10.1103/PhysRevD.9.3320.

[106] S. Weinberg, Phys. Rev. D **9** (1974) 3357–3378, doi:10.1103/PhysRevD.9.3357.

[107] L. Jacobs, Phys. Rev. D **10** (1974) 3956, doi:10.1103/PhysRevD.10.3956.

[108] U. Wolff, Phys. Lett. B **157** (1985) 303–308, doi:10.1016/0370-2693(85)90671-9.

[109] T. Inagaki, T. Kouno, and T. Muta, Int. J. Mod. Phys. A **10** (1995) 2241–2268, doi:10.1142/S0217751X95001091, arXiv:hep-ph/9409413.

[110] T. M. Apostol, *"Introduction to Analytic Number Theory"*, Springer, New York, US, 1976, pp. 257–259.

[111] D. K. Kim, Y. D. Han, and I. G. Koh, Phys. Rev. D **49** (1994) 6943–6946, doi:10.1103/PhysRevD.49.6943.

[112] A. Roberge and N. Weiss, Nucl. Phys. B **275** (1986) 734–745, doi:10.1016/0550-3213(86)90582-1.

[113] K. Kashiwa, Symmetry **11** (2019) no. 4, 562, doi:10.3390/sym11040562.

[114] J. Lenz, L. Pannullo, M. Wagner, B. Wellegehausen, and A. Wipf, Phys. Rev. D **101** (2020) no. 9, 094512, doi:10.1103/PhysRevD.101.094512, arXiv:2004.00295 [hep-lat].